Automotive FMCW Radar With Difference Co-Chirps

LIFAN XU, Student Member, IEEE
SHUNQIAO SUN, Senior Member, IEEE
The University of Alabama, Tuscaloosa, AL USA

KUMAR VIJAY MISHRA, Senior Member, IEEE
U.S. DEVCOM Army Research Laboratory, Adelphi, MD USA

YIMIN D. ZHANG, Fellow, IEEE
Temple University, Philadelphia, PA USA

In an automotive radar scenario, the transmission of sparsely spaced chirps along *slow time* creates opportunities to significantly reduce or completely avoid mutual interference. However, nonuniform chirps result in high Doppler sidelobes, which may introduce ambiguity in Doppler estimation. In this article, we present an automotive frequency-modulated continuous-wave radar that exploits difference co-chirps to achieve high-accuracy range–Doppler estimation with low complexity. By exploiting sparsity in *slow time*, the proposed method achieves the same Doppler velocity resolution as the regular uniform pulsing but with much fewer chirps. The silent transmission intervals become available to other automotive radars, thereby eliminating the mutual interference. The *fast-time* samples are treated as *snapshots* to construct the second-order statistical information for Doppler spectrum estimation. For our proposed nonuniform pulsing, we develop an efficient range–Doppler spectrum estimation method and propose a matching technique that is based on 2-D compressed sensing followed by Doppler dealiasing. This algorithm achieves *ipso facto* range–Doppler pairing without grid mismatch errors in parameter estimation and does not require an exhaustive search. Extensive numerical experiments show that accurate range–Doppler estimation is achieved with significantly fewer chirps compared to the conventional consecutive transmission. Field campaigns using Texas Instruments imaging radar support our theoretical investigations.

Manuscript received 4 May 2022; revised 7 October 2022, 20 March 2023, and 19 July 2023; accepted 23 July 2023. Date of publication 27 July 2023; date of current version 8 December 2023.

DOI. No. 10.1109/TAES.2023.3299259

Refereeing of this contribution was handled by I. Bilik.

This work was supported in part by the U.S. National Science Foundation under Grant CCF-2153386 and in part by the Alabama Transportation Institute. An earlier version of this paper was presented at the 2021 IEEE International Conference on Autonomous Systems (ICAS) [DOI: 10.1109/ICAS49788.2021.9551195].

Authors' addresses: Lifan Xu and Shunqiao Sun are with the Department of Electrical and Computer Engineering, The University of Alabama, Tuscaloosa, AL 35487 USA, E-mail: (lxu36@crimson.ua.edu; shunqiao.sun@ua.edu); Kumar Vijay Mishra is with the U.S. DEVCOM Army Research Laboratory, Adelphi, MD 20783 USA, E-mail: (kumar-vijay-mishra@uiowa.edu); Yimin D. Zhang is with the Department of Electrical and Computer Engineering, Temple University, Philadelphia, PA 19122 USA, E-mail: (ydzhang@temple.edu). *(Corresponding author: Shunqiao Sun.)*

I. INTRODUCTION

Automotive radar sensors are fundamental to advanced driver assistance systems and modern autonomous vehicles largely because of their inexpensive circuitry, ability to sense during inclement weather, and immunity to poor visibility conditions [2], [3], [4], [5], [6]. Most practical automotive radar systems employ frequency-modulated continuous-wave (FMCW) transmit signals at the millimeter-wave band to achieve low-cost high-resolution sensing for complex functions in autonomous driving, such as automatic emergency braking, blind-spot detection, and adaptive cruise control [7], [8]. The deployment of such radars operating in the same frequency range of 76–81 GHz in dense traffic scenarios has led to concerns regarding severe mutual interference from one radar to another.

Mutual interfering signals lead to widespread contamination of range–Doppler spectrum and degrade radar's performance [5], [9]. Among several studies that address the automotive radar interference problem [9], notching out the contaminated samples at the receiver is a common practice, which, however, leads to signal distortion and reduced resolution [10]. On the transmit side, the interference can be addressed by transmitting well-designed radar signals that are nearly orthogonal to each other in the spectral/temporal domains [9] at the cost of additional time/frequency slots. In this article, we focus on transmit-centric approaches that address the aforementioned problems.

An alternative to traditional orthogonal transmission is to employ nonuniform chirps (along *slow time*) and recover target parameters, such as target range and Doppler (velocity), through sparse construction techniques [11], [12], [13]. This allows automotive radars to utilize the media access control [14], [15], [16] for transmission coordination. However, radars with nonuniform pulse repetition intervals (PRIs) [17] are known to suffer from high sidelobe levels along slow time as a result of undersampling. In [17], a weight interpolation technique was considered to handle the high sidelobes in the Doppler spectrum caused by nonuniform pulsing. In [18], after performing interpolation to suppress these sidelobes, the nonuniform pulses are processed via nonuniform fast Fourier transform (NUFFT). The direct interpolation of Fourier coefficients is avoided in [12] by employing the compressed sensing (CS) technique to recover the Doppler information. An optimal pulse transmission structure and sampling rules were considered in [19] to control the sidelobe level of the Doppler spectrum.

When the number of sparse nonuniform chirps during one coherent processing interval (CPI) is much smaller than the number of chirps in consecutive uniform transmission, the corresponding high sidelobes in the Doppler spectrum can hardly be reduced by using the above approaches [11],

[12], [13], [17], [18], [19]. Hence, further investigation on nonuniform pulsing is required to design accurate slow-time sparse structures for automotive radar signals. In this context, it is instructive to investigate the concept of difference coarrays [20] in the slow-time domain. By utilizing the coarray structure, difference coarrays greatly increase the number of spatial degrees of freedom of the corresponding physical arrays to achieve more effective direction-of-arrival estimation.

There are several variants of sparse arrays, including minimum redundancy array [21], [22], nested array [23], [24], and coprime array [20], [25], [26], that are suited to effectively construct difference coarrays. In a wide-sense stationary (WSS) process scenario, missing elements (i.e., holes) in the difference coarrays can be interpolated to form a virtual uniform linear array if the snapshots are sufficient [27]. Very recently, Lv et al. [28] have extended coarrays to a joint spatiospectral domain for a frequency-diverse array radar through coprime chirp pulsing by a coprime physical array to achieve joint range–Doppler–angle estimation. However, in automotive radar scenarios, the WSS assumption across multiple CPIs and multiple snapshots is not always guaranteed because of the highly dynamic and high-speed target environment [5], [29].

In this article, we develop the concept of difference co-chirps for the automotive radar that leaves a silent interval in the CPI so that other automotive radars can emit signals with negligible interference. We obtain the ambiguity functions (AFs) of our proposed automotive radar waveforms under two representative difference co-chirp transmissions, i.e., coprime and nested. In the difference co-chirp transmission, the estimation of target Doppler velocity becomes challenging because of spectral ambiguity and difficulty in pairing the target Doppler with the corresponding range. We address these challenges by constructing the second-order covariance matrix for Doppler spectrum estimation using fast Fourier transform (FFT) with the fast-time samples used as snapshots. Our 2-D CS approach then pairs targets' range and Doppler, followed by Doppler dealiasing. We further improve the performance through an efficient *boosted* pairing algorithm that leverages the information obtained from the FFT stage to avoid CS grid mismatch errors [30], [31] and the need for an exhaustive blind search. Extensive numerical results validate our model and methods. Finally, we demonstrate the practical feasibility of difference co-chirp transmission and parameter recovery through field experiments using a Texas Instruments (TI) radar setup.

The basic concept of the co-chirp scheme was presented in [1] with preliminary simulation results on the joint range and Doppler estimation. The substantive novel contributions of this article beyond [1] include a detailed analysis of the AFs of the co-chirp waveforms, the development of the boosted algorithm, more comprehensive numerical studies, and verification based on field experiment results.

The rest of this article is organized as follows. In Section II, we briefly describe the conventional FMCW radar processing and then generalize the difference coarray concept to difference co-chirps for automotive FMCW radar. In Section III, the AFs of difference co-chirps transmissions are derived for performance analysis. The range–Doppler reconstruction method and pairing techniques to construct the 2-D range–Doppler spectrum are presented in Section IV. We validate our models and methods with extensive numerical and field experiments in Section V. Finally, Section VI concludes this article.

Throughout this article, uppercase and lowercase bold characters denote matrices and vectors, respectively. Matrix vectorization operation is denoted by $\mathrm{vec}(\cdot)$. The conjugate transpose is $(\cdot)^H$ and conjugate is denoted by $(\cdot)^*$. The complex values set is $\mathbb{C}$. The function $\lceil\cdot\rceil$ yields the smallest integer that is greater than or equal to its argument. The notation $\odot$ denotes the Kronecker product.

II. SYSTEM MODEL

Conventional automotive sensing is based on the FMCW radar, which offers very high-range resolutions unmatched by contemporary pulse-Doppler radars and high resilience to the negative effects of target Doppler. This is very useful in obtaining cleaner displays with low clutter and tracking fast targets in automotive scenarios. The focus of this article is the detection of only high-speed targets. Clutter being a low Doppler scatterer is, therefore, not considered in our model. The clutter encountered in lane change assist, blind-spot detection, and tune assist are not considered in this article. Note that stationary clutter is generally observed at a very low depression angle yielding insignificant backscattering. The clutter is typically homogenous with concentrated Doppler frequencies corresponding to the platform' speed, which is known to the radar. As such, the clutter may be easily mitigated. Usually, clutter returns tend to be composed of discrete scatterers, such as walls, vegetation, and traffic signs. The literature suggests that space-time adaptive processing (STAP) is effective in removing both periodic [32] and nonperiodic [33] clutter in road environments. Whereas these methods were proposed for conventional uniform chirp transmission strategies, the authors in [34], [35], and [36] have previously considered STAP-based clutter suppression for nested/coprime structures and are applicable to our approach.

A. Uniform Pulse Repetition Frequency FMCW Radar

Consider a monostatic FMCW radar that emits a linear frequency ramp [see Fig. 1(a)] with bandwidth B, duration time T, and carrier frequency f_c. The transmit signal for one ramp at the mth chirp is

$$x(m,t) = \mathrm{rect}\left(\frac{t-mT_p}{T}\right) e^{j2\pi\left[f_c+\frac{B}{T}(t-mT_p)\right](t-mT_p)} \quad (1)$$

where $T_p = 1/f_{\mathrm{PRF}}$ is the uniform PRI, f_{PRF} is the pulse repetition frequency (PRF), and the rectangular pulse window function is defined as

$$\mathrm{rect}\left(\frac{t-\tau}{T}\right) = \begin{cases} 1, & \tau \le t \le \tau + T \\ 0, & \text{otherwise} \end{cases}. \quad (2)$$

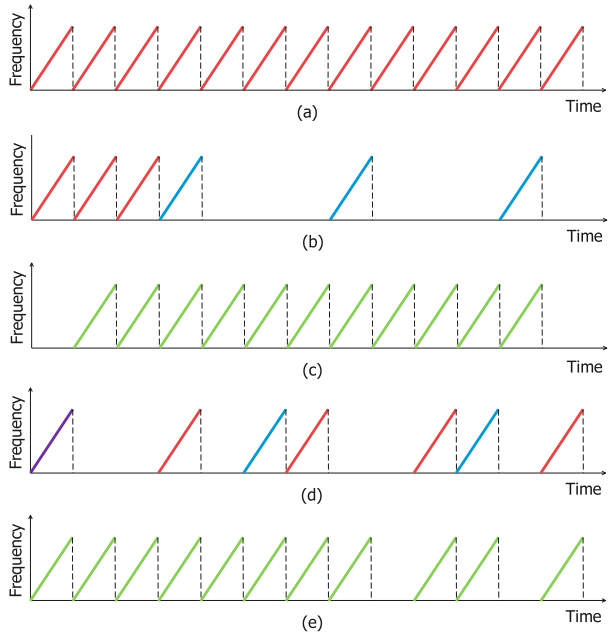

Fig. 1. Nonuniform chirps transmission sequences and their difference co-chirps. The missing chirp indices are left blank, and the filled difference chirp indices are denoted by green sawtooth waveform. (a) Uniform PRF chirps. (b) Nested chirps transmission sequence for $N_1 = 3$ and $N_2 = 3$. (c) Interpolated chirps in nested transmission. (d) Coprime chirp transmission sequence for $N_1 = 3$ and $N_2 = 5$. (e) Interpolated chirps in coprime transmission.

After integration, the phase of the transmit signal $x(m, t)$ becomes

$$\begin{aligned}\varphi_T\left(t - mT_p\right) &= 2\pi \int_{mT_p}^{mT_p+t} \left[f_c + \frac{B}{T}(t - mT_p)\right] dt \\ &= 2\pi \left(f_c t + \frac{1}{2} \cdot \frac{B}{T} t^2\right) - \varphi_{T_0} \end{aligned} \tag{3}$$

where φ_{T_0} depends on the PRI T_p.

Assume K signals within the radar's effective field of view. The noise-free received signal $y(m, t)$ is a weighted delayed version of $x(m, t)$, expressed as

$$y(m, t) = \sum_{k=1}^{K} \alpha_k e^{j2\pi\left[f_c(t-\tau_k)+\frac{B}{2T}(t-\tau_k)^2-\varphi_{T_0}\right]} \tag{4}$$

where α_k denotes the reflection coefficient of signal with delay τ_k.

The emitted signal $x(m, t)$ is used to dechirp the received signal $y(m, t)$ to generate the *beat signal*, whose phase is

$$\Delta\varphi(t) = \varphi_T(t) - \varphi_T(t - \tau_k) = 2\pi \left(f_c\tau_k + \frac{B}{T} t\tau_k - \frac{B}{2T}\tau_k^2\right) \tag{5}$$

where t is the fast time with $0 \le t \le T$, and τ_k characterizes the delay between the transmitted signal and the received signal of the kth target. The quadratic term of τ_k is negligible in (5) because $\tau_k/T \ll 1$ holds in short-range automotive radar.

To unfold the delay time τ_k, consider the kth target located at range r_k away from the radar and moving with a constant velocity v_k. Then, the round-trip transmission delay for the kth target is $\tau_k = 2(r_k + v_k t)/c$, where c is the speed of light. The phase of the dechirped signal is

$$\Delta\varphi(t) = 2\pi \left[\frac{2f_c r_k}{c} + \left(\frac{2f_c v_k}{c} + \frac{2Br_k}{cT}\right) t + \frac{2Bv_k}{cT} t^2\right]. \tag{6}$$

The last term can be neglected for a similar reason $t/T \ll 1$. The term $2f_c r_k/c$ does not change with the fast time and is only associated with the range and, therefore, can be absorbed into the reflection coefficient. Simplifying, the resulting *beat frequency* is

$$f_b^k = \frac{2f_c v_k}{c} + \frac{2Br_k}{cT} = f_D^k + f_R^k \tag{7}$$

where $f_D^k = 2f_c v_k/c$ and $f_R^k = 2Br_k/(cT)$ are the Doppler and range frequencies of the kth target, respectively.

In automotive radars, the maximum detection range is typically several hundreds of meters, and therefore, $f_b \ll B$ holds. As a result, the beat signals are sampled using a relatively inexpensive low-rate analog-to-digital converter. Denote the sampling interval in the fast time by T_A and $1/T_A > 2f_b^{\max}$, where $f_b^{\max}$ denotes the maximum beat frequency. Then, the ith sample in the mth chirp becomes

$$y(m, i) = \sum_{k=1}^{K} \alpha_k e^{j2\pi\left(f_b^k iT_A + f_D^k mT_p\right)} \tag{8}$$

where $f_D mT_p = 2f_c v_k T_p m/c$ denotes the Doppler frequency change in the mth chirp. The CPI consists of M chirps, and the number of samples in each chirp is I. The sampled automotive radar data matrix of a channel is $\mathbf{Y} \in \mathbb{C}^{I\times M}$, whose (m, i)th entry is denoted as $y(m, i)$.

In most automotive radar scenarios, $f_D \ll f_R$ holds [5]. Thus, the Doppler frequency f_D is negligible when a single chirp is considered. However, for the high-range-resolution radar, this term should be compensated to realize a high range accuracy. The target range is estimated by applying FFT to fast-time samples in the abovementioned data matrix. For each range bin, the range frequency f_R is constant across the slow time. Therefore, the Doppler is estimated by applying FFT along the slow time in data matrix $\mathbf{Y}$ [5]. To avoid ambiguity in the Doppler spectrum estimation in a uniform PRF radar, it is required that $f_{\text{PRF}} \ge 2f_D^{\max}$, where $f_D^{\max}$ denotes the maximum Doppler frequency.

B. Difference Co-Chirp-Based FMCW Radar

Consider a uniformly spaced chirp set $\mathcal{S} = \{m_1, m_2, \ldots, m_M\}$, which has M entries with m_i describing the position of the ith chirp. The difference co-chirp set is

$$\mathcal{S}_{\text{diff}} = \{m_i - m_j\} \qquad \forall i, j \in \mathcal{S}. \tag{9}$$

In this definition, $\mathcal{S}_{\text{diff}}$ does not allow the repetition of its elements, i.e., all the entries have distinct values.

1) *FMCW Radar With Nested Chirps:* We now examine the FMCW radar that schedules its slow-time emission following the nested-chirp relationship. Two-level chirp indices are used in the basic nested-chirp transmission.

Specifically, the first and second levels consist of N_1 and N_2 chirps with corresponding PRIs as T_p and $(N_1+1)T_p$, respectively. Here, two integers N_1 and N_2 are selected to realize a reasonable Doppler resolution. Under the nested chirps, the FMCW radar transmits chirps at slow-time indices as per the set

$$\mathcal{S}_{\text{nested}} = \{1, 2, \ldots, N_1, (N_1+1), 2(N_1+1), \ldots, N_2(N_1+1)\}. \tag{10}$$

The set $\mathcal{S}_{\text{diff}} = \{n_1 - n_2 | n_1, n_2 \in \mathcal{S}_{\text{nested}}\}$ is called the difference set of nested chirps, where the total number of the transmitted chirps is $N = N_1 + N_2$.

Under the nested transmission, the first N_1 transmitted chirps have a PRI of T_p, while the other N_2 chirps have a PRI of $(N_1+1)T_p$. The sampled beat signal at the mth chirp is (8) for $m \in \mathcal{S}_{\text{nested}}$. Following (8), the ith snapshot of slow-time samples or the ith row of the sparse radar matrix is

$$\mathbf{y}^i_{\text{nested}} = \mathbf{B}\boldsymbol{\Sigma}\mathbf{s}^i + \mathbf{n}^i \tag{11}$$

where $\mathbf{B} = [\mathbf{b}(f_D^1), \ldots, \mathbf{b}(f_D^K)] \in \mathbb{C}^{N\times K}$ is the Doppler manifold with $\mathbf{b}(f_D^k) = [e^{j2\pi f_D^k T_p}, \ldots, e^{j2\pi f_D^k N T_p}]^T$ and $\mathbf{s}^i = [e^{j2\pi f_b^k i T_A}, \ldots, e^{j2\pi f_b^k i T_A}]^T$. Here, $\mathbf{n}^i$ denotes the addictive white Gaussian noise vector in the ith snapshot of slow-time samples and $\boldsymbol{\Sigma} = \text{diag}([\alpha_1, \ldots, \alpha_K])$.

2) *FMCW Radar With Coprime Chirps:* A classical coprime structure is illustrated in Fig. 1(d), where N_1 and N_2 are two coprime integers that define a chirp slow-time slot set as

$$\mathcal{S}_{\text{coprime}} = \{N_1(n_2-1), 1 \leqslant n_2 \leqslant N_2\} \cup \{N_2(n_1-1), 1 \leqslant n_1 \leqslant N_1\}. \tag{12}$$

An FMCW signal is transmitted at the slow-time indices specified in the above coprime set and the total number of the transmitted chirps is $N = N_1 + N_2 - 1$ because of the shared first chirp. The difference co-chirps set is

$$\mathcal{S}_{\text{diff}} = \{s_1 - s_2 | s_1, s_2 \in \mathcal{S}_{\text{coprime}}\}. \tag{13}$$

However, the difference co-chirp set does not provide consecutive chirps between time slots $-N_2(N_1-1)$ and $N_1(N_2-1)$, so certain chirp indices are missing [see Fig. 1(e)].

Under the nested transmission, the transmitted chirps are scheduled following the transmission set $\mathcal{S}_{\text{coprime}}$. The sampled beat signal at the mth chirp is (8) for $m \in \mathcal{S}_{\text{coprime}}$.

Following a similar procedure as the nested transmission, we also obtain the ith row $\mathbf{y}^i_{\text{coprime}}$ for the coprime scheme.

C. Advantages of Sparse Transmissions

The advantages of sparse transmission in slow time manifest in several ways.

1) *High Doppler Resolution Using Few Chirps:* The Doppler velocity resolution Δv is determined by the length of a CPI, $\Delta v = c/(2f_c M T_p)$. To achieve the same Doppler resolution as a uniform PRF, an FMCW radar under the difference co-chirp needs to sparsely occupy the whole CPI along the slow time following the corresponding coprime or nested co-chirp rules. Fig. 1(a) illustrates a case where a total of 13 chirps are transmitted under the uniform PRF in one CPI. In comparison, for the same observation interval, only seven and six chirps are needed under the coprime and nested-chirp strategies, respectively.

2) *Significantly Reduced Interference to Victim Radar Through Sparse Transmission:* The sparse transmission along slow time significantly reduces the probability a victim radar would be interfered compared to the uniform transmission scheme since much fewer chirps of the victim radars could be potentially corrupted. As the interference sample's amplitude is stronger than the target echo, the interference can be further suppressed by adopting the simple thresholding/gating approach [5] to mitigate the interference before carrying out 2-D FFT for range–Doppler estimation. The gating approach is chosen as the baseline method for interference mitigation due to simplicity and relative good performance [5]. Fig. 12 illustrates an example of the interference gating.

3) *Support Multiple Radars' Simultaneous Transmission With Low Interference:* The proposed sparse transmission in slow time offers opportunistic transmission for other automotive radars with only a small fraction of pulses being interfered. To take advantage of these silent opportunities, these radars must coordinate with the host radar using vehicle-to-vehicle communication [37], such as dedicated short-range communication [38]. Then, time synchronization between radars can be realized by the global positioning system (GPS) technology or atomic clock technology [39], [40], [41]. For example, pulse-per-second signals from two GPS modules achieve 60-ns accuracy in synchronization [42]. More specifically, timing and carrier frequency synchronization in the case of distributed radar systems, as is the case with vehicular traffic scenarios, may also be achieved through the use of existing communications protocols [43], two-way time transfer [44], and multitone frequency transfer [45].

To analyze the maximum number of radars that can transmit sparsely at the same time, we consider a simple example where all the radars follow the same transmission pattern but with different starting times. In the nested transmission scheme, there are $N = N_1 + N_2$ chirps. In the first level, N_1 chirps will be transmitted with PRI $= T_p$. In the second level, N_2 chirps will be transmitted with PRI $= (N_1+1)T_p$. Therefore, there are $N_2 - 1$ slots available for other radars to transmit signals, and each slot duration is $N_1 T_p$. The maximum number of radars that can simultaneously transmit is N_2. Here, we define the collision rate as

$$cr = \mu/(N_1 + N_2) \tag{14}$$

where μ denotes the number of collided chirps. A simple example of $N_1 = 3$ and $N_2 = 3$ is shown in Fig. 2(a). In this case, starting from the second CPI, most of the radars will have $\mu = N_2$ overlapping chirps with each other, and thus, the collision rate is $cr = N_2/(N_1 + N_2) = 0.5$.

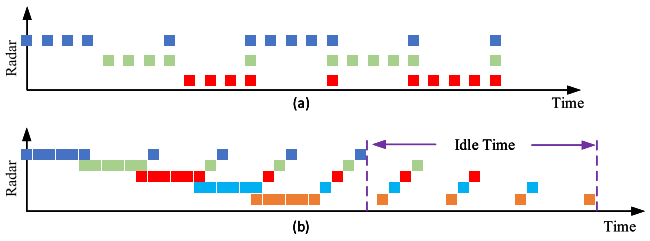

Fig. 2. Nonuniform chirps transmission sequences and their maximum transmission capacity simultaneously. The different colors block denote the different radars. (a) Maximum transmission capacity with full silence slots usage. (b) Incremental transmission strategy with fewer collisions.

To reduce the collision rate, an incremental schedule to support N_t radars to transmit simultaneously with a short idle time of $(N_t - 1)N_1T_p$ is proposed. Fig. 2(b) illustrates an example of the schedule of $N_t = 5$ radars, each using the nested scheme of $N_1 = 5$ and $N_2 = 5$. In this schedule, an idle time is introduced to allow all N_t radars to complete one CPI transmission. The number of maximum overlapping chirps is $\mu = N_t - 1 = 4$, and thus, the collision rate can be small. For example, to support five radars to transmit simultaneously with $N_1 = N_2 = 17$, the collision rate is $cr = \mu/(N_1 + N_2) = 4/34 = 0.117$. A thorough simulation is carried out in Section V-B, and the results are shown in Fig. 14.

It is worth noting that other radars can exploit the silent periods without necessarily adhering to the same difference co-chirps as we illustrated in this article. For instance, by transmitting irregular sparse chirps, utilizing compressive sensing for Doppler estimation may achieve better performance [46], [47].

D. Detection Performance With Respect to Signal-to-Noise Ratio

The U.S. Federal Communications Commission [48] recommends that the peak and average power densities of automotive radar systems operating in 76–77 GHz are, respectively, less than 2.79 and 0.88 W/m^2, at a distance of 3 m. The typical transmit power of automotive radar systems is around 1 W [5]. It is reported in [49] that the power density is 0.88 W/m^2 at 3 m for a radio source with transmit power of 2 W, which is much smaller than 10 W/m^2 suggested by the International Commission on Nonionizing Radiation Protection (ICNIRP) [50].

Sparse transmission along slow time results in reduced SNR, which may lead to detection performance degradation under low-signal-to-noise ratio (SNR) scenarios compared to uniform transmission. A thorough simulation under different SNRs has been conducted in Section V-A, and the result is shown in Fig. 11. This performance degradation under low SNRs is common for radar systems employing sparse signal processing [11], [12], [13]. Under high-SNR scenarios, the difference co-chirp has comparable performance to the conventional uniform transmission.

A feasible approach to achieving comparable detection performance to that of conventional transmission is to increase the transmit power of each chirp in the sparse transmission, while still satisfying the power density requirement suggested by the ICNIRP. By doing so, the transmit signal can reach greater distances, subsequently increasing the likelihood of interference with a larger number of victim radars. Assuming the same total transmit power for sparse and uniform transmissions, the worst case is that the total interference power received by a victim radar under both sparse and uniform transmissions will be the same. Again, thresholding/gating can help mitigate the interference with a higher amplitude experienced at the victim radar. In Section V-B, we conduct a thorough performance comparison of victim radar under sparse and uniform transmissions, and the results shown in Fig. 15 demonstrate significant performance improvement of the proposed difference co-chirp scheme over the uniform transmission counterpart, since much fewer chirps are corrupted and strong interference signals due to increased transmit power are efficiently mitigated by gating.

III. AFS OF AUTOMOTIVE RADARS WITH DIFFERENCE CO-CHIRP

The radar AF is an important tool for waveform design and analysis that succinctly describes the behavior of a waveform paired with its matched filter. The AF is useful for the analysis of the resolution, sidelobe behavior, and ambiguities in both range and Doppler domains for a given waveform, as well as phenomena such as range–Doppler coupling [51], [52]. The AFs of classical continuous-wave waveforms, such as linear frequency-modulated (FM) or single-frequency signals for uniform PRF, have been investigated thoroughly in the literature [53]. In Theorem 1, we derive the AFs for the nested and coprime transmissions.

THEOREM 1 Consider a rectangular pulse with duration of T that has the AF

$$A(t, f_d) = \left| \left(1 - \frac{|t|}{T}\right) \frac{\sin\left[\pi f_d(T - |t|)\right]}{\pi f_d(T - |t|)} \right|, \quad |t| \leqslant T \tag{17}$$

where f_d denotes the Doppler frequency. Consider a nested-chirp transmission formed by two groups of chirps N_1 and N_2 with respective PRIs T and $\hat{T} = (N_1 + 1)T$, and a coprime chirp transmission formed by two overlapped group chirps of coprime numbers N_1 and N_2 with respective PRIs T_1 and T_2. The AFs under nested and coprime transmissions are expressed in (15) and (16), shown at the bottom of the next page, respectively.

PROOF See the Appendix. □

The unambiguous Doppler interval of nested AF is nonuniform, and it is minimum and maximum intervals are $1/\hat{T}$ and $1/T$, respectively. The unambiguous range interval is bounded by $[T, \hat{T}]$. The minimum unambiguous Doppler interval of coprime AF is $\min(1/T_1, 1/T_2)$, and its maximum

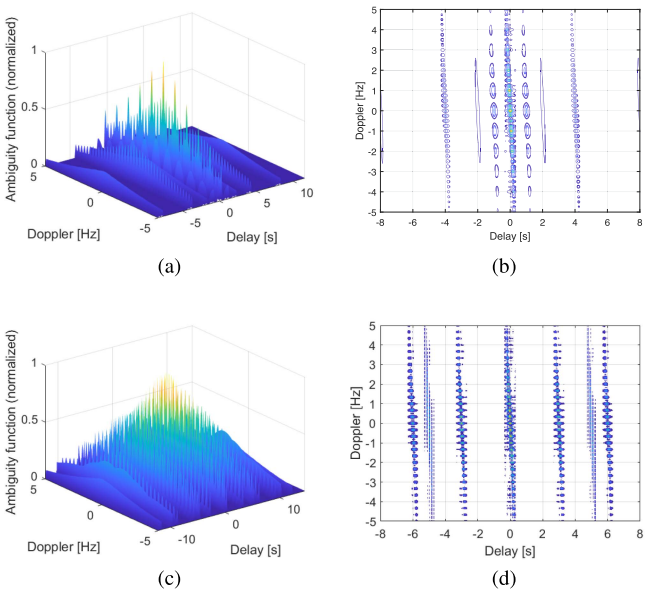

Fig. 3. (a) AF of nested-chirp transmission sequence. (b) Same as (a) but shown in a contour plot. (c) and (d) Same as (a) and (b), respectively, but for coprime chirp transmission sequence.

is $\max(1/T_1, 1/T_2)$. The unambiguous range interval of coprime AF is bounded by $[\min(T_1, T_2), \max(T_1, T_2)]$.

Fig. 3 shows an example of the nested-chirp AF in the top panel. The first (second) group of chirps have $N_1 = 3$ ($N_2 = 3$) pulses with the PRI of 1 s (4 s). This results in a dwell time of 12 s. Fig. 3(a) and (b) shows that the nested chirp possesses the same Doppler resolution as the uniform one, and its unambiguous range interval and unambiguous Doppler interval are limited by the PRIs of the inner and outer group chirps, respectively. Similarly, the bottom panel of Fig. 3 plots the coprime-chirp AF, where the PRI of the first (second) group with $N_1 = 3$ ($N_2 = 5$) pulses is 1 s (5 s). Fig. 3(c) and (d) illustrates that the unambiguous range interval is confined by the PRI difference between N_1 and N_2, and the unambiguous Doppler interval is limited by the PRI of N_2 group chirps. Fig. 3 demonstrates that, compared with coprime, the nested-chirp transmission does not change the maximum unambiguous range and Doppler interval, and its sidelobes decay faster than the coprime transmission. However, the coprime technique narrows down the unambiguous Doppler interval because of nonconsecutive chirps in the transmission.

Since the difference co-chirp following the coprime transmission results in some missing data in the full dwell time after slow-time interpolation, an intuitive way is to truncate the dwell time to maintain a consecutive slow-time sequence. However, this degrades the velocity estimation performance because of a shorter CPI. A more effective alternative is to interpolate these missing data via the Toeplitz matrix completion approaches [54], [55] using the second-order statistical information. The matrix completion-based interpolation approach requires a high SNR to guarantee bias-free interpolation. However, the input SNR of the raw echo data in the automotive radar is relatively low (usually less than 0 dB) [5]. In this context, the nested co-chirp transmission is more favorable than the coprime counterpart because of its nonhole feature in the whole CPI duration after slow-time interpolation.

IV. RANGE–DOPPLER–ANGLE RECOVERY

In a uniform PRF FMCW radar, performing a 2-D FFT on the beat signal directly yields paired range and Doppler information. However, when the transmission sequence is sparse, this technique is both inapplicable and inaccurate [11]. We address these shortcomings by developing a Doppler estimation procedure with difference co-chirps based on the second-order statistics of radar samples. This is followed by an efficient pairing strategy for range–Doppler parameters.

A. Doppler Estimation With Difference Co-Chirps

In each CPI, we interpolate the missing samples along the slow time for Doppler estimation via the construction of a second-order covariance matrix. Such interpolation requires a large number of snapshots. As mentioned earlier in Section II-A, the Doppler shift in a typical automotive radar is negligible during fast-time sampling of a single chirp and is viewed as a constant [5]. Therefore, we treat the fast-time samples as "snapshots" for Doppler covariance

$$A_{\text{nested}}(t, f_d) = \sum_{n_1=-(N_1-1)}^{N_1-1} A\left(t - n_1 T, f_d + \frac{B}{T}t\right)\left|\frac{\sin(\pi(f_d + \frac{B}{T}t)(N_1 - |n_1|)T)}{\sin(\pi(f_d + \frac{B}{T}t)T)}\right| + \sum_{n_2=-(N_2-1)}^{N_2-1} A\left(t - n_2\hat{T}, f_d + \frac{B}{\hat{T}}t\right)\left|\frac{\sin(\pi(f_d + \frac{B}{\hat{T}}t)(N_2 - |n_2|)\hat{T})}{\sin(\pi(f_d + \frac{B}{\hat{T}}t)\hat{T})}\right|. \tag{15}$$

$$A_{\text{coprime}}(t, f_d) = \sum_{n_1=-(N_1-1)}^{N_1-1} A\left(t - n_1 T_1, f_d + \frac{B}{T_1}t\right)\left|\frac{\sin(\pi(f_d + \frac{B}{T_1}t)(N_1 - |n_1|)T_1)}{\sin(\pi(f_d + \frac{B}{T_1}t)T_1)}\right| + \sum_{n_2=-(N_2-1)}^{N_2-1} A\left(t - n_2 T_2, f_d + \frac{B}{T_2}t\right)\left|\frac{\sin(\pi(f_d + \frac{B}{T_2}t)(N_2 - |n_2|)T_2)}{\sin(\pi(f_d + \frac{B}{T_2}t)T_2)}\right|. \tag{16}$$

matrix construction. The sampling Doppler covariance matrix is

$$\begin{aligned}\mathbf{R}_{\text{nested}} &= \frac{1}{I}\sum_{i=1}^{I}\mathbf{y}^i_{\text{nested}}\left(\mathbf{y}^i_{\text{nested}}\right)^H \\ &= \frac{1}{I}\sum_{i=1}^{I}\left[\mathbf{B}\boldsymbol{\Sigma}\mathbf{s}^i(\mathbf{s}^i)^H\boldsymbol{\Sigma}^H\mathbf{B}^H + \mathbf{n}^i\left(\mathbf{n}^i\right)^H\right] \\ &= \mathbf{B}_n\mathbf{R}_\alpha\mathbf{B}_n^H + \sigma_n^2\mathbf{I}. \end{aligned} \tag{18}$$

For the same range bin, the term $\mathbf{s}^i(\mathbf{s}^i)^H = \mathbf{I}$, where $\mathbf{I}$ is an identity matrix and I is the number of fast-time samples, which means the fast-time information embedded in f_b will be dismissed in the covariance matrix and only Doppler-related samples will be extracted. By vectorizing $\mathbf{R}_{\text{nested}}$, the co-chirp signal model is

$$\mathbf{r}_{\text{nested}} = \text{vec}(\mathbf{R}_{\text{nested}}) = \left(\mathbf{B}_n^* \odot \mathbf{B}_n\right)\mathbf{p} + \sigma_n^2\mathbf{i} \tag{19}$$

where $\mathbf{p} = (\alpha_1^2, \ldots, \alpha_K^2)^T$ and $\mathbf{i} = \text{vec}(\mathbf{I})$.

The Doppler autocorrelation $\mathbf{y}^i_{\text{nested}}(\mathbf{y}^i_{\text{nested}})^H$ is composed of entries including $e^{j2\pi f_D^k(n_2-n_1)T_p}$ for $n_1, n_2 \in \mathcal{S}_{\text{nested}}$, i.e., $e^{j2\pi f_D^k n T_p}$ for $n \in \mathcal{S}_{\text{diff}}$. It follows from the properties of the nested chirps that the indices in $\mathcal{S}_{\text{diff}}$ are consecutive for a given observation interval $N_1(N_2-1)T_p$, and therefore, the missing Doppler samples along the slow time can be interpolated via the Doppler autocorrelation. The number of averaged unique consecutive Doppler samples $\mathbf{d}^{\text{UC}}_{\text{diff}} = \text{unique}(\mathbf{r}_{\text{nested}})$ is obtained from the sampling covariance vector with indices defined in $\mathcal{S}_{\text{diff}}$.

The Doppler spectrum is then obtained by applying FFT to the interpolated Doppler samples along the slow time. The Doppler spectrum is accurate and robust, which also reveals the targets' power as the diagonal elements of $\mathbf{R}_\alpha = \boldsymbol{\Sigma}\boldsymbol{\Sigma}^H = \text{diag}([\alpha_1^2, \ldots, \alpha_K^2])$. In a similar way, the decoupled range and Doppler spectrum can also be estimated using the coprime transmission strategy. However, due to the coprime chirp properties, the coprime transmission fashion cannot enjoy the consecutive Doppler samples for the same dwell time as the conventional transmission scheme after slow-time interpolation.

For single-range multiple-Doppler or single-Doppler multiple-range scenarios, the cross-spectrum displays the target position and velocity information. However, for multiple target scenarios, the cross-range–Doppler spectrum would yield redundant peaks arising from the decoupling between the range and the velocity. Fig. 4 shows an example of the range–Doppler spectrum based on the unpaired range and velocity results under nested co-chirp transmission with $N_1 = N_2 = 17$ and $T_p = 15$ μs. Two targets with the same radar cross section (RCS) at ranges of $r_1 = 45$ m and $r_2 = 87.5$ m, and corresponding velocities of $v_1 = 35$ m/s and $v_2 = 10$ m/s are considered in the simulation.

B. Joint Range–Doppler Estimation

Sparse sampling in the Doppler domain yields high sidelobes in the Doppler spectrum posing a challenge in correctly pairing range and Doppler parameters in the nested transmission. Consider the following example: There are three targets in the field of view of the radar, and their range–velocity pairs are [45 m, 10 m/s], [87.5 m, 10 m/s], and [45 m, 35 m/s], respectively. The reflection coefficients of the three targets are normalized to $\alpha_1 = 0.3$, $\alpha_2 = 0.5$, and $\alpha_3 = 1$ and assumed to be unchanged during the processing interval. As shown in Fig. 5, the weaker target (target 1 with $\alpha_1 = 0.3$ and range–velocity pair [45 m, 10 m/s]) is buried in the high sidelobes of the targets with larger RCS and, therefore, difficult to detect. It means that the range and Doppler results obtained from FFT cannot be directly used to detect the true target positions. To this end, we now present our *co*-chirp joint range-*D*oppler estimation with *D*opp*Dler* dealiasing (CoDDler) super-resolution algorithm. The first step of this technique employs 2-D CS to jointly estimate the range and Doppler using sparse samples along the slow-time. In the second step, we remove the Doppler ambiguity through a difference co-chirps interpolation-based Doppler dealiasing strategy.

Denote the maximum detection range and the maximum velocity by R_u and $v_{\max}$, respectively. To construct an appropriate CS dictionary [56], [57], we discretize range and Doppler into a fine grid with $M_r \times M_v$ points. This

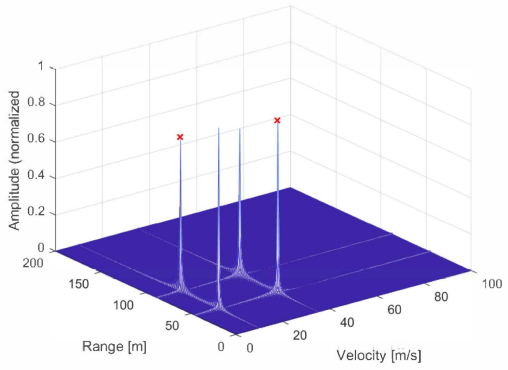

Fig. 4. Range–Doppler spectrum based on the unpaired results. The true locations (marked by ×) of the targets in the range–Doppler plane are $\{r_1 = 45$ m, $v_1 = 35$ m/s$\}$ and $\{r_2 = 87.5$ m, $v_2 = 10$ m/s$\}$.

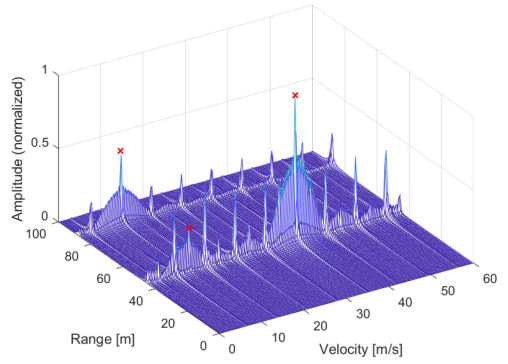

Fig. 5. Range–Doppler spectrum of nested co-chirp transmission with three targets.

results in the corresponding range and Doppler grid sizes of R_u/M_r and $2v_{\max}/M_v$, respectively. The ξth range and ηth discretized velocity are denoted as R_ξ and v_η, respectively. The corresponding beat frequency is $f_b^{\xi\eta} = f_R^\xi + f_D^\eta$. Denote the noise-free data matrix by $\mathbf{Z}_{\xi\eta} \in \mathbb{C}^{I\times N}$, whose (n, i)th element is

$$z(n,i) = e^{j2\pi\left(f_b^{\xi\eta} iT_A + f_D^\eta nT_p\right)}, \quad n \in \mathcal{S}_{\text{nested}}. \tag{20}$$

The dictionary of the 2-D CS is

$$\mathbf{A} = \left[\text{vec}\left(\mathbf{Z}_{11}\right), \ldots, \text{vec}\left(\mathbf{Z}_{1M_v}\right), \text{vec}\left(\mathbf{Z}_{21}\right), \ldots, \text{vec}\left(\mathbf{Z}_{M_rM_v}\right)\right]. \tag{21}$$

In practice, the measurement is corrupted by additive noise leading to $\text{vec}(\mathbf{Y}) = \mathbf{Ax} + \mathbf{n}$, where $\mathbf{n}$ is the noise vector. Here, $\mathbf{x} \in \mathbb{C}^{M_vM_r\times 1}$ is a sparse vector, where $x_j = \alpha_h$ with $h = K_u$ or $h = P_c$ if the hth target has range of $\frac{R_u}{M_r}\left\lceil \frac{j}{M_v}\right\rceil$ and velocity of $-v_{\max} + \frac{2v_{\max}}{M_v} \bmod (j, M_r)$; otherwise, $x_j = 0$.

We obtain the unknown range and Doppler by solving the following relaxed ℓ_1-norm optimization:

$$\text{minimize } \|\mathbf{x}\|_1 \quad \text{subject to } \|\text{vec}(\mathbf{Y}) - \mathbf{Ax}\|_2 \le \delta \tag{22}$$

where δ is the noise bound. The signal vector $\mathbf{x}$ in (22) may be estimated through popular solvers such as Dantzig selector [58] or orthogonal matching pursuit (OMP) [59]. In general, for the successful recovery of the sparse vector $\mathbf{x}$, the dictionary matrix $\mathbf{A}$ must satisfy certain properties dictated by CS theory, e.g., low value of mutual coherence [60], defined as

$$\mu(\mathbf{A}) = \max_{l\ne j} \frac{\left|\mathbf{a}_l^H\mathbf{a}_j\right|}{\|\mathbf{a}_l\|_2\left\|\mathbf{a}_j\right\|_2} \tag{23}$$

where $\mathbf{a}_j$ denotes the jth column of matrix $\mathbf{A}$.

For nested (and, similarly, for coprime) transmission, there are two subchirp sequences with two different uniform PRIs. Using the similar phase conjugation in [61], the $(r; v)$-dependent range–Doppler pattern is written as

$$\varphi(r; v) = \sum_{n=0}^{N_1+N_2-1}\sum_{i=0}^{I-1} z^*(r_i; v_n)\, z(r; v). \tag{24}$$

The range–Doppler pattern has a peak value when $r_i = r$ and $v_n = v$. The $\mathbf{a}_l^H\mathbf{a}_j$ for $l \ne j$, represents the energy leakage of the range–Doppler steering vector pointing at $(r_l; v_l)$ to range and velocity bins of $(r_j; v_j)$. Thus, $\max_{l\ne j}|\mathbf{a}_l^H\mathbf{a}_j|$ corresponds to the peak sidelobe of the range–Doppler pattern. Let $\Delta_r = r_l - r_j$, $\Delta_v = v_l - v_j$, and $T_{p2} = (N_1 + 1)T_p$. Equations (25) and (26) shown at the bottom of the this page, hold. It is clear that the mutual coherence $\mu(\mathbf{A})$ is a parameter-dependent value. For given system parameters, its value reaches a maximum $I(N_1 + N_2)$ when Δ_r and Δ_v approach to zero. The mutual coherence will decrease when Δ_r and Δ_v take larger values. Equation (26) reveals that the peak sidelobe appear around the real target leading to inaccurate detections. Therefore, a dealiasing in range and Doppler is necessary.

To illustrate the parameter-dependent mutual coherence, we plot the mutual coherence of the radar dictionary as a function of discretized grid size of the range and the Doppler in Fig. 6 with parameters given in Table I, and the grid steps are set to the same along the range and Doppler axes. It follows that the mutual coherence is highly correlated with the discretized grid step of the velocity and

TABLE I
Radar Parameters

Parameters	Values
Carrier frequency, f_c	77 GHz
Maximum detection range, $R_{\max}$	200 m
Maximum detection velocity, $V_{\max}$	230 km/h
Bandwidth, B	150 MHz
Pulse duration, T_d	7.3 μs

$$\begin{aligned}
\mathbf{a}_l^H\mathbf{a}_j &= \sum_{n_1=0}^{N_1-1}\sum_{i=0}^{I-1} e^{j2\pi\left(f_b^l iT_A + f_D^l n_1T_p\right)} e^{-\text{j}2\pi\left(f_b^j iT_A + f_D^j n_1T_p\right)} + \sum_{n_2=0}^{N_2-1}\sum_{i=0}^{I-1} e^{j2\pi\left(f_b^l iT_A + f_D^l n_2T_{p2}\right)} e^{-\text{j}2\pi\left(f_b^j iT_A + f_D^j n_2T_{p2}\right)} \\
&= \sum_{n_1=0}^{N_1-1}\sum_{i=0}^{I-1}\left\{e^{j2\pi\left[\frac{2B}{cT}(r_l-r_j)+\frac{2f_c}{c}(v_l-v_j)\right]iT_A} e^{j2\pi\left[\frac{2f_c}{c}n_1T_p(v_l-v_j)\right]}\right\} + \sum_{n_2=0}^{N_2-1}\sum_{i=0}^{I-1}\left\{e^{j2\pi\left[\frac{2B}{cT}(r_l-r_j)+\frac{2f_c}{c}(v_l-v_j)\right]iT_A} e^{j2\pi\left[\frac{2f_c}{c}n_2T_{p2}(v_l-v_j)\right]}\right\} \\
&= \frac{1-\left[e^{j2\pi\left(\frac{2B}{cT}\Delta_r+\frac{2f_c}{c}\Delta_v\right)T_A}\right]^I}{1-e^{j2\pi\left(\frac{2B}{cT}\Delta_r+\frac{2f_c}{c}\Delta_v\right)T_A}} \times \frac{1-\left[e^{j2\pi\frac{2f_c}{c}\Delta_vT_p}\right]^{N_1}}{1-e^{j2\pi\frac{2f_c}{c}\Delta_vT_p}} + \frac{1-\left[e^{j2\pi\left(\frac{2B}{cT}\Delta_r+\frac{2f_c}{c}\Delta_v\right)T_A}\right]^I}{1-e^{j2\pi\left(\frac{2B}{cT}\Delta_r+\frac{2f_c}{c}\Delta_v\right)T_A}} \times \frac{1-\left[e^{j2\pi\frac{2f_c}{c}\Delta_vT_{p2}}\right]^{N_2}}{1-e^{j2\pi\frac{2f_c}{c}\Delta_vT_{p2}}}.
\end{aligned} \tag{25}$$

$$\begin{aligned}
\left|\mathbf{a}_l^H\mathbf{a}_j\right| &= \left|\frac{\sin\left[\pi\left(\frac{2B}{cT}\Delta_r+\frac{2f_c}{c}\Delta_v\right)T_AI\right]}{\sin\left[\pi\left(\frac{2B}{cT}\Delta_r+\frac{2f_c}{c}\Delta_v\right)T_A\right]}\right| \times \left|\frac{\sin\left(\pi\frac{2f_c}{c}\Delta_vT_pN_1\right)}{\sin\left(\pi\frac{2f_c}{c}\Delta_vT_p\right)} + \frac{\sin\left(\pi\frac{2f_c}{c}\Delta_vT_{p2}N_2\right)}{\sin\left(\pi\frac{2f_c}{c}\Delta_vT_{p2}\right)}\right| \\
&= \left|I\frac{\text{sinc}\left[\left(\frac{2B}{cT}\Delta_r+\frac{2f_c}{c}\Delta_v\right)T_AI\right]}{\text{sinc}\left[\left(\frac{2B}{cT}\Delta_r+\frac{2f_c}{c}\Delta_v\right)T_A\right]}\right| \times \left|N_1\frac{\text{sinc}\left(\frac{2f_c}{c}\Delta_vT_pN_1\right)}{\text{sinc}\left(\frac{2f_c}{c}\Delta_vT_p\right)} + N_2\frac{\text{sinc}\left(\frac{2f_c}{c}\Delta_vT_{p2}N_2\right)}{\text{sinc}\left(\frac{2f_c}{c}\Delta_vT_{p2}\right)}\right|.
\end{aligned} \tag{26}$$

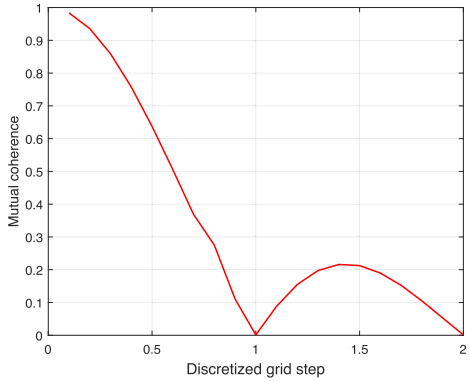

Fig. 6. Mutual coherence of the dictionary matrix with respect to the discretized grid step in range and Doppler domains.

Algorithm 1: *Co*-Chirp Joint Range-*D*oppler Estimation With *Dopp*ler Dealiasing.

Input: N_1, N_2, M_v, M_r, and the received sparse data matrix $\mathbf{Y}$.
Output: dealiasing CS range–Doppler spectrum.
Doppler spectrum with interpolated Doppler samples:
1: $\mathbf{R}_{\text{nested}} = \frac{1}{I}\sum_{i=1}^{I} \mathbf{y}^i_{\text{nested}} (\mathbf{y}^i_{\text{nested}})^H$.
2: $\mathbf{d}^{\text{UC}}_{\text{diff}} = \text{unique}(\mathbf{r}_{\text{nested}})$.
3: $\mathcal{D} = \text{FFT}\{\mathbf{d}^{\text{UC}}_{\text{diff}}\}$.
Range-Doppler estimation with 2-D CS and Doppler dealiasing:
4: Discretize the range and velocity into a fine grid and construct dictionary matrix $\mathbf{A}$ according to (21).
5: Solve ℓ_1-norm optimization problem (22) by OMP.
6: Apply the Doppler spectrum $\mathcal{D}$ to filter out spurious velocity peaks in CS estimation.

the range. In order to obtain a high range and Doppler resolutions, a finer local discretized gridding in the range and the velocity is beneficial. However, such a small grid step results in high mutual coherence and, subsequently, high sidelobes of the Doppler spectrum. Algorithm 1 summarizes these steps.

Although the co-chirp joint range–Doppler estimation with Doppler dealiasing pairs range and Doppler correctly with a high resolution, the computation cost is relatively high. Moreover, the matching error highly depends on the way the dictionary is constructed. For instance, if the discretized grid is small enough, the matching error will be less significant. However, according to the mutual coherence analysis of the dictionary, a small discretized step leads to a larger mutual coherence value, which worsens the sidelobe level in the range–Doppler spectrum and requires high computer memory demand. Inevitably, the inherent off-grid problem also results in pairing errors.

The cost of solving the l_1-norm optimization problem (22) by OMP is $\mathcal{O}(\dim(\mathbf{A})G)$, where $\dim(\mathbf{A})$ is the size

Algorithm 2: *B*oost Co-chirp joint range-*D*oppler estimation with *Dopp*ler dealiasing (BoDDler).

Input: $r_{\text{fft}}, v_{\text{fft}}, \mathcal{D}$ and the received sparse data matrix $\mathbf{Y}$.
Output: dealiasing CS range–Doppler spectrum.
1: Construct dictionary matrix $\mathbf{A}_r$ according to (21).
2: Solve ℓ_1-norm optimization problem (22) by OMP.
3: Apply the Doppler spectrum $\mathcal{D}$ to filter out fake velocity peaks in CS estimation.

of dictionary matrix $\mathbf{A}$ and G denotes the number of iterations [62]. In this application, the size of a conventional dictionary matrix $\mathbf{A}$ is $IN \times M_r M_v$. The need for high-resolution sensing requires the discretized steps in M_r and M_v directions to be kept small, leading to prohibitively high computational costs. For example, storing several gigabytes for dictionary matrix $\mathbf{A}$ is impractical for many embedded systems. To mitigate such problems, we propose a minimum dictionary size-based Doppler dealiasing and pairing procedure. The candidate set of range $r_{\text{fft}} = \{r_1, r_2, \ldots, r_K\}$ is captured very well by FFT along fast-time sampling with threshold techniques. After performing FFT on consecutive interpolated Doppler samples obtained from the sampling covariance matrix, the velocity candidate set $v_{\text{fft}} = \{v_1, v_2, \ldots, v_J\}$ can also be estimated. Thus, the reduced-size dictionary matrix $\mathbf{A}_r$ is

$$\mathbf{A}_r = \left[\text{vec}(\mathbf{Z}_{r_1 v_1}), \text{vec}(\mathbf{Z}_{r_2 v_1}), \ldots, \text{vec}(\mathbf{Z}_{r_k v_j})\right], \quad r_k \in r_{\text{fft}}, v_j \in v_{\text{fft}}. \tag{27}$$

This *b*oosted version of CoDDler algorithm (BoDDler) is summarized in Algorithm 2.

The dimension of the dictionary matrix $\mathbf{A}_r$ in the BoDDler is at most $IN \times KJ$. Because $KJ \ll M_r M_v$, the computation cost of BoDDler is $\mathcal{O}(INKJG)$. The computation cost of the BoDDler is much less than the computation complexity of the original version, where typically $M_r M_v$ is quite large (say 10^4) to realize a high resolution. One additional advantage of the BoDDler is that it does not require grid discretization because all detected range and Doppler results are given to build the dictionary, which totally avoids the off-grid issue inherent in CS [30] and the resolution limitation depends only on the fast-time and slow-time Fourier transforms. The matching guarantee is based on the fact that $\mathbf{A}_r$ is still an overcomplete dictionary and contains all atoms of the original signal.

After obtaining a range estimate from range FFT, one could apply 1-D CS [58], [59], [63] along the slow time for each range to automatically pair the range and the Doppler. However, this approach does not exploit the known velocity information obtained from slow-time FFT along the interpolated slow-time samples and, therefore, requires a longer time for the matching process.

Conventional CS methods do have the ability to retrieve information from sparse (nonuniform) sampling. A straightforward nonuniform sampling could be random, but it must

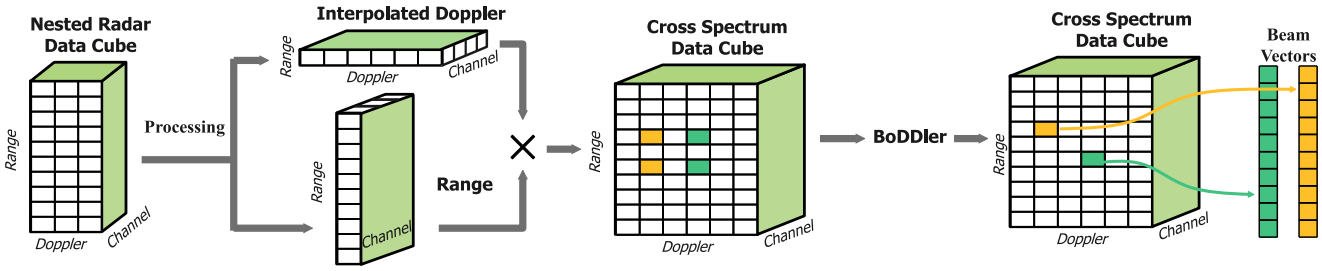

Fig. 7. Illustration of the beam vector extraction from a nested radar data cube.

be properly designed to keep a low mutual coherence in the dictionary and a low computational complexity. The coarray-based chirping is more structured and, therefore, easy to implement in hardware when compared to random pulsing, which usually leads to higher sidelobes. Moreover, basic co-chirp processing may be used as a template for analyzing other nonuniform pulsing methods (see [28, Sec. V.C] for some examples). Using the coarray method, we can use the fast-time samples as snapshots, so that the Doppler information is recovered by exploiting the coarray feature. Combining the velocity and the range, the pairing procedure becomes more cost-effective.

C. Direction Finding and Extension to 4-D High-Resolution Imaging Radar

An application of the automotive radar with difference co-chirps to a 4-D high-resolution imaging radar in range, Doppler, azimuth, and elevation is shown in Fig. 7. For each channel, the interpolated Doppler spectrum $\mathbf{SP}(\mathbf{d}_{\text{diff}}^{\text{UC}}) \in \mathbb{C}^{\text{N}_{\text{vfft}}\times 1}$ is obtained by performing N_{vfft}-point FFT along the interpolated Doppler. Following the same trace, the range spectrum $\mathbf{SP}(\text{R}) \in \mathbb{C}^{\text{N}_{\text{rfft}}\times 1}$ is the result of performing N_{rfft}-point FFT along the fast-time samples. Therefore, the cross spectrum is obtained as $\mathbf{SP}(\text{CP}) = \mathbf{SP}(\text{R}) \times \mathbf{SP}(\mathbf{d}_{\text{diff}}^{\text{UC}})^{\text{T}} \in \mathbb{C}^{\text{N}_{\text{rfft}}\times \text{N}_{\text{vfft}}}$. For specific target locations, the indexes in the range–Doppler spectrum corresponding to the actual target positions are obtained from the BoDDler algorithm. These true positions are aligned with the cross spectrum to select the actual angle information cell p_n^i of the ith target for the nth channel, where $i \in [1, 2, \ldots, P]$ and $n \in [1, 2, \ldots, N]$. After performing this procedure for all channels and target locations, the actual angular cells are stacked according to their channel index order to form the array manifold $\mathbf{A}_{\text{angle}} \in \mathbb{C}^{N\times P}$, which is then used to perform direction finding. Depending on the array geometry and the availability of array snapshots, direction finding can be carried out using FFT or high-resolution subspace methods, such as MUSIC [64], ESPRIT [65], or CS [58], or iterative adaptive approach [66].

For driver-over and driver-under functions [7], 2-D antenna arrays deployed in both horizontal and vertical directions are required to support joint azimuth and elevation direction finding. The angular resolution is determined by the antenna array aperture, i.e., $\Delta_\theta = 2\arcsin(1.4\lambda/(\pi D))$, where λ is the wavelength corresponding to the carrier frequency and D is the aperture size of the receiver array. As a result, the hardware cost of 4-D imaging radar is high if full arrays of large apertures are adopted for joint azimuth and elevation direction finding. To reduce the hardware complexity while achieving the same angular resolution as a full-array counterpart, different strategies are available to design 2-D sparse arrays in the context of multi-input multi-output radar [5]. For example, to enable high-resolution 4-D imaging, the authors in [7] and [67] proposed to exploit a joint sparsity design in frequency spectrum and array configurations. There are several off-the-shelf 4-D imaging radar prototypes, such as TI cascade imaging radar [68], and commercial automotive radar products, such as Continental ARS540 [69]. However, the detailed discussion of 2-D sparse array design and direction finding is out of the scope of this article.

V. NUMERICAL AND FIELD EXPERIMENT RESULTS

We carried out numerical and radar field experiment results to evaluate the performance of the proposed difference co-chirps waveform. Table I lists the settings of a radar system consisting of a single transmitter and 20 uniformly deployed 1-D linear receivers used in our experiments.

A. Parameter Retrieval Without Interference

To realize the maximum unambiguous detectable velocity requirement listed in Table I, the PRI is bounded by $T_p = 15\ \mu$s. To determine the target velocities, for conventional FMCW radar, a total number of 306 uniform chirps are transmitted in one CPI, and the dwell time is $NT_p = 4.59$ ms. Consequently, the velocity resolution is $\Delta v = \lambda/(2NT_p) = 0.42$ m/s. Two targets are considered with ranges $r_1 = 87.5$ m and $r_2 = 45$ m, velocities $v_1 = 10$ m/s and $v_2 = 35$ m/s, and azimuth angles $\theta_1 = 15^\circ$ and $\theta_2 = 37^\circ$. The reflection coefficients of the two targets are normalized to $\alpha_1 = 0.5$ and $\alpha_2 = 1.0$ and are assumed to be unchanged during the processing interval. The input SNR is set to 0 dB.

In order to achieve the same dwell time as the conventional one to maintain the velocity resolution, the nested co-chirp transmission suggests that the first uniform pulse train has $N_1 = 17$ chirps with the same repetition interval T_p as in the traditional transmission, and the second uniform pulse train transmits a total number of $N_2 = 17$ pulses with

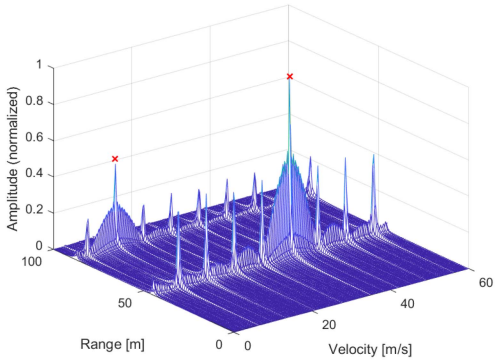

(a)

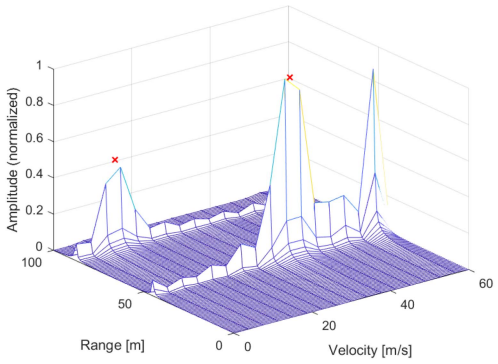

(b)

Fig. 8. Range–Doppler spectrum on sparse data under nested co-chirp transmission. (a) 2-D FFT. (b) 2-D nonuniform FFT. The red × denotes the actual positions of the targets.

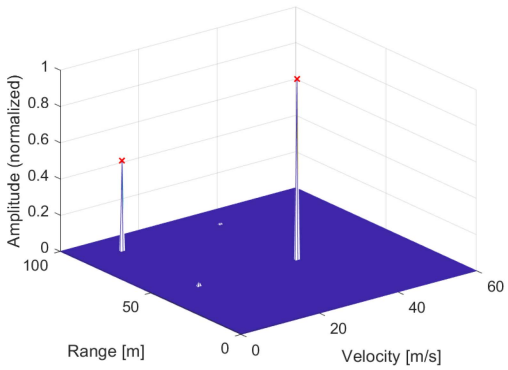

(a)

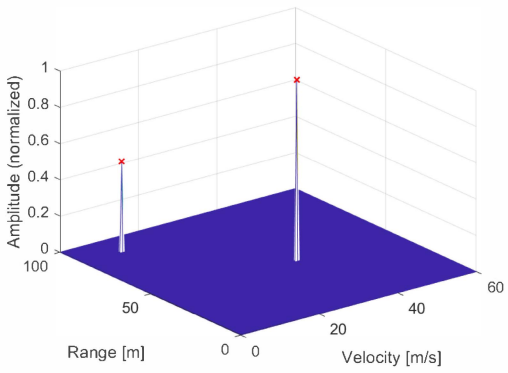

(b)

Fig. 9. 2-D boosted CS on sparse data. (a) Initial pairing. (b) After amplitude dealiasing. The red × denotes the actual positions of the targets.

PRI of $T_{P_2} = (N_1 + 1)T_p$. For the coprime transmission, the coprime pair is $N_1 = 17$ and $N_2 = 18$.

Under the nested transmission, the FFT spectrum performed on the received sparse data directly is shown in Fig. 8(a), where it can be found that the high sidelobes of the strong target would bury targets with weaker reflection coefficients, thereby reducing the radar probability of detection (PD). Another classical technique to perform FFT on nonuniform sampling data is the nonuniform FFT [18]. Fig. 8(b) shows the 2-D spectrum obtained by applying NUFFT on only 11% of the original uniform sampling data. And it can be found that the high sidelobe levels still stand out and may mask targets with weaker reflection coefficients.

With the range and Doppler estimates obtained by applying FFTs on, respectively, fast-time and interpolated slow-time samples, the pairing is achieved by the 2-D boosted-CS method. Certain spurious peaks appear in the 2-D boosted-CS spectrum because of the overestimation of the number of targets, as shown in Fig. 9(a). To remove these, the target magnitude and velocity set $\mathcal{D}$ is used to filter out noise-like peaks in the 2-D boosted-CS spectrum. After dealiasing, a perfect spectrum is available in Fig. 9(b). It should be noted for 2-D boosted CS of carrying range and Doppler pairing, the atoms in the dictionary are constructed from the estimations in the set of r_{fft} and v_{fft}. Therefore, the resolution of 2-D boosted CS depends on the number of points used in the FFT.

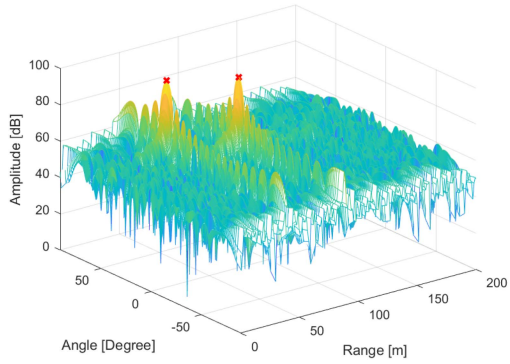

Fig. 10. Direction finding using nested co-chirp from a 20-element uniform linear array, where × denotes the ground truth.

The beam vector $\mathbf{p}^I$ for each target was obtained by alignment of the clean positioning output of the 2-D enhanced CS with the prepossessed cross-range–Doppler spectra of each channel. Applying FFT along each beam vector is an efficient method for target angle analysis. As shown in Fig. 10, two targets can be accurately estimated.

To statistically evaluate the recovery performance of the nested co-chirp, we apply the hit or missing criterion [13]

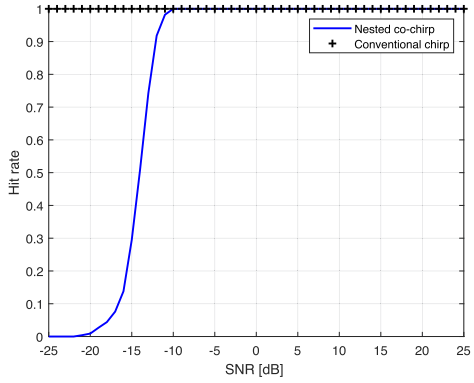

(a)

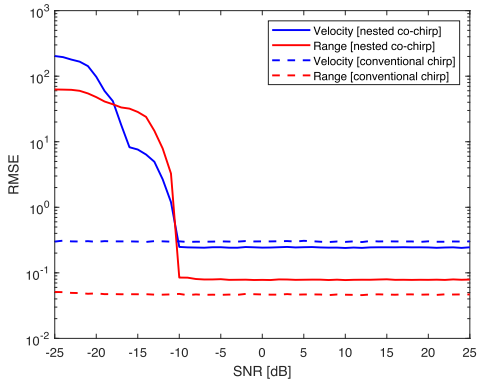

(b)

Fig. 11. Performance comparison between conventional and nested co-chirp transmissions. (a) Hit rate comparison. (b) RMSE of range and velocity for conventional (dashed lines) and nested (solid lines) transmissions.

to examine the range–Doppler recovery rate under different input SNR values. Here, a hit denotes that the absolute error of the recovered range–Doppler pair is within the range and Doppler resolutions. For comparison, we also show the recovered hit rate of the conventional chirp transmission scheme. We placed two targets with normalized reflection coefficients of $\alpha_1 = 0.5$ and $\alpha_2 = 1.0$, which remain unchanged during the processing interval. The velocity and range of these two targets are drawn uniformly at random from [10, 90] m/s and [10, 100] m, respectively. For each input SNR selected from 11 uniformly spaced values in the interval $[-25, 25]$ dB, we perform 1000 Monte Carlo simulations. As shown in Fig. 11(a), the hit rate reaches unity when the input SNR is above -10 dB. The root-mean-squared error (RMSE), defined as $\text{RMSE} = \sqrt{\sum_{i=1}^{M_c}(\hat{y}_i - y_i)^2/M_c}$ using M_c independent trials, is used as the performance metric to measure the deviation of the detection result $\hat{y}$ from the ground truth y. Here, $\hat{y}$ and y denote either velocity or range estimation and their corresponding ground truth values, respectively. All the detection results for conventional and nested co-chirp schemes are obtained from the same (2048×2048)-point FFTs along the range and the Doppler dimensions. Fig. 11(b) shows that the RMSEs of the range and velocity estimates under the nested co-chirp are close to those obtained from a conventional uniform chirp transmission when SNR is larger than -10 dB. The number of points of FFT along fast time or slow time bounds the estimation errors.

Under the nested co-chirp transmission, we use the fast-time samples as snapshots to construct a covariance matrix, based on which the missing data containing Doppler information along slow time can be interpolated. Then, FFT is applied to these interpolated data to retrieve the target velocity spectrum. The velocity and the range spectra are plotted in Fig. 13(a) and (c), respectively, which perfectly match the ground truth. Therefore, these detected range and Doppler peaks can be imported to a 2-D boosted-CS algorithm for pairing. However, for the coprime transmission, the interpolated data are not consecutive in the whole dwell time. The few missing slow-time slots lead to energy leakage on the velocity spectrum when performing FFT on the interpolated data. Fig. 13(b) shows the slow-time FFT spectrum based on the interpolated data under the coprime transmission, and the consequence of energy leakage appears in a form of high sidelobes. Targets with weaker reflection coefficients have the risk of being buried by the high sidelobes. Since the mutual coherence of the dictionary matrix is high, the 2-D CS technique is not guaranteed to find correct range–Doppler estimation without reliable Doppler dealiasing. Therefore, the nested-chirp transmission is superior to its coprime counterpart.

B. Parameter Retrieval in the Presence of Interference

It is of great interest to see the performance of automotive radar under difference co-chirp transmissions when there is interference, i.e., there is no transmission coordination among multiple radars. The radar parameters remain the same as those used in Section V-A. The interference duration at certain chirps is given by $T_i = |2f_b^{\max}/(S_i - S)|$, where $f_b^{\max}$ denotes the maximum beat frequency and S_i and S are the chirp slopes of the interference and the victim radars, respectively [5]. The signal-to-interference-plus-noise ratio (SINR) of the mth chirp is defined as $\text{SINR} = 10\log10(\|\mathbf{y}(:, \text{m})\|_2/(\|\Lambda\|_2) + \|\mathbf{n}\|_2)$, where Λ contains the interference samples collected within the interference duration and $\mathbf{n}$ denotes the noise vector. To investigate the interference signal, we set the input SNR $= 0$ dB to define the fixed input noise level. After dechirping and low-pass filtering, the received signal consists of signal and interference trails, as shown in Fig. 12(a). Since the interference signal comes from a direct path, it has stronger power than the target echoes. As shown in Fig. 12(b), the noise floor of the range–Doppler spectrum increases significantly due to the interference.

It is imperative to evaluate the performance of the proposed automotive radar under the nested-chirp transmission using the receiver operating characteristic (ROC) curve for different SINR settings. In the simulation, the interference is generated following the above worst case setting. Five targets are located at a range between 10 and 90 m. Their normalized reflection coefficients vary between $\alpha_1 = 0.5$

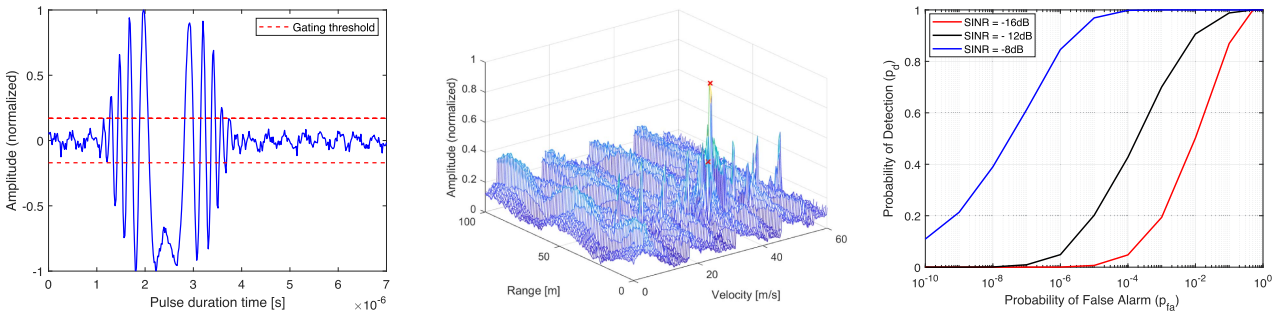

(a) (b) (c)

Fig. 12. Performance under interference. (a) Fast-time samples under the nested transmission with SINR $= -12$ dB. (b) Range–Doppler spectrum with SINR $= -12$ dB. (c) ROC curve under different SINRs in the worst case interference setting.

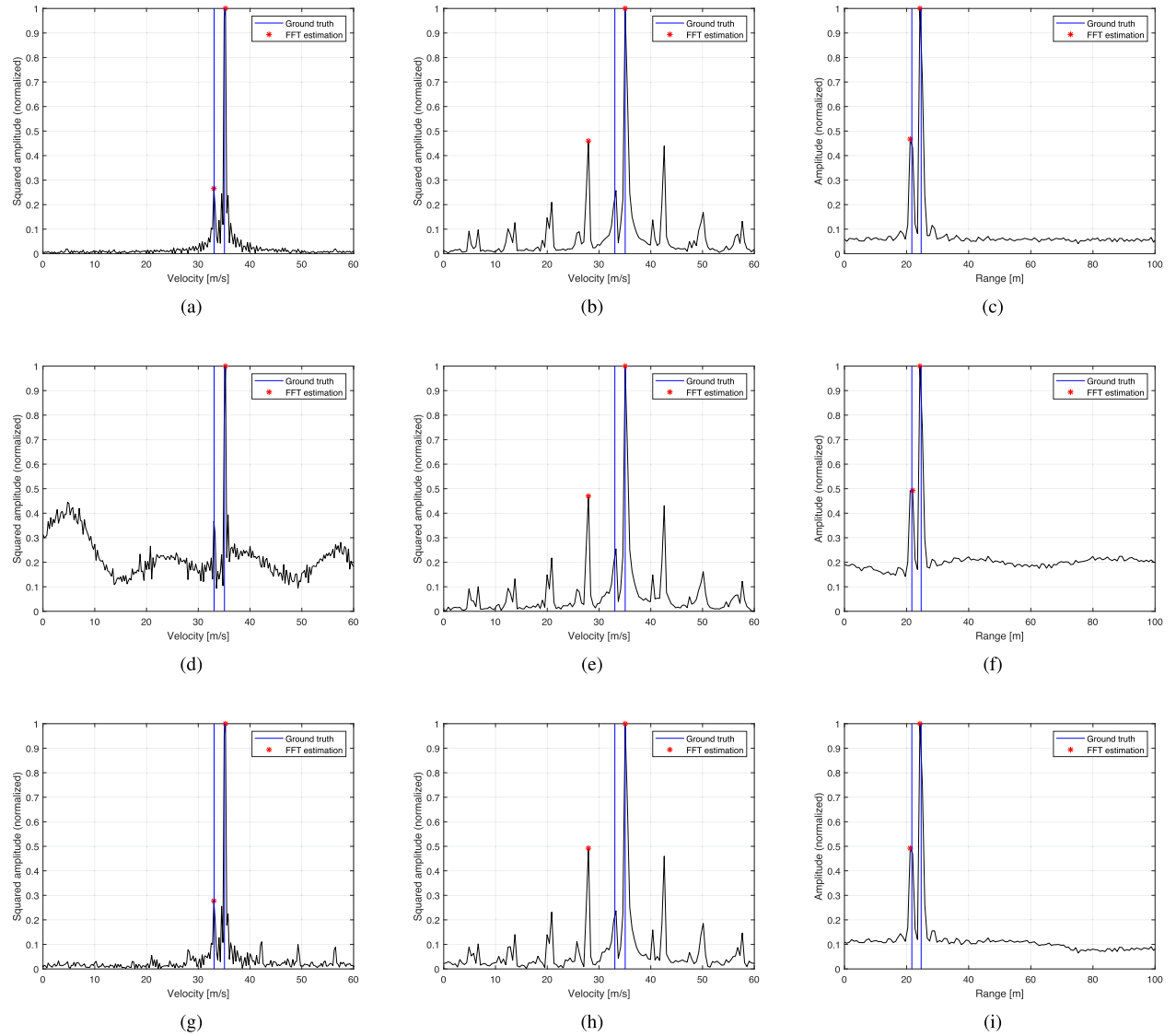

(a) (b) (c)

(d) (e) (f)

(g) (h) (i)

Fig. 13. Performance comparison between (a)–(c) without interference, (d)–(f) with interference of SINR $= -12$ dB appearing continuously with a duration equivalent to the first 30 chirps, and (g)–(i) with interference of SINR $= -12$ dB appearing sparsely at random along the whole CPI. Doppler estimation with FFT: (a), (d), and (g) Nested transmission; (b), (e), and (h) coprime transmission; and (c), (f), and (i) range estimation with FFT under the nested transmission.

TABLE II
Parameters of Interfering Radar

Parameter	Value
Distance	$10-40$ m
Bandwidth	$[0.6-1.05]B$ MHz
Pulse duration	$[0.9-1.35]T_d$ μs
PRI_i	$[0.9-1.35]\text{PRI}$ μs

and $\alpha_2 = 1$. The input INR varies between -16 and -8 dB with a step size of 4 dB, and a total number of 3000 independent trials are carried out to compute the averaged PD and probability of false alarm (PFA). Each range–Doppler map has 512×512 samples. Here, a successful detection means that both the ranges and velocities of the five targets are correctly estimated. During each trial, the velocity difference between the two targets is at least 1 m/s, and the range difference between the two targets is more than 1 m/s. Fig. 12(c) shows that, for SINR $= -16$ dB, only under higher PFAs, the five targets are detected successfully. When SINR $= -8$ dB, the PD is close to 1 for a small PFA, i.e., 10^{-4}.

We consider the worst interference scenario that the interference appears continuously in a duration equivalent to the first 30 chirps. It is clear that the first subgroup chirps of the victim radar under the nested-chirp transmission would be contaminated by this type of interference. As shown in Fig. 13(d) and (f), the noise floor in both Doppler and range spectra raise drastically compared with those in Fig. 13(a) and (c) without interference. However, the effect of this continuous interference appearing in the first few chirps is less significant for victim radar under the coprime transmission because less number of chirps are contaminated. As shown in Fig. 13(e), the noise floor of the Doppler spectrum under the coprime transmission increases slightly compared with the result in Fig. 13(b) without interference. We then consider the other interference scenarios, for instance, when an interference appears sparsely at random along the whole CPI. Fig. 13(g)–(i) indicates that the influence of this type of interference is less significant because the victim radar under the difference co-chirps remains silent for most of the time during one CPI. As a result, the chance of receiving interference is greatly reduced. If there is interference, it only appears in a few chirps.

To evaluate the performance of detection with different interfering parameters, we conduct Monte Carlo simulations with a total number of 3000 independent runs to assess the hit rate of the victim radar. In the experiment, the victim radar has the following parameters, i.e., $B = 150$ MHz, $T_d = 7.33$ μs, and PRI $= 9.76$ μs. The parameters of interfering radar with FMCW waveforms are given in Table II, and the incident azimuth angle of interfering radar is always at $\theta_i = 0^\circ$. In each run, the interfering radar's bandwidth, pulse duration, PRI, and distance to the victim radar are randomly drawn from the feasible region given in Table II. The simulation result is shown in Fig. 14, where we observe that if the collision occurs in the sparse transmission stage and, hence, $cr < 0.5$ (e.g., we use $cr = 0.12$ in the simulations), the hit rate reaches to unity when the SINR exceeds -10 dB. A partial collision scenario ($cr = 0.5$) requires SINR to be higher than -7 dB to reach similar hit rates. Simultaneous transmission during all chirps, i.e., the full collision case ($cr = 1$), requires SINR to be up to -5 dB to reach the unity hit rate. However, full collision situation does not frequently occur, and the nested co-chirp offers good anti-interference performance in most cases.

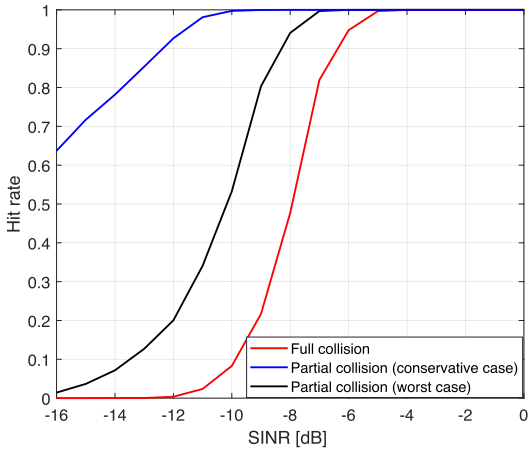

Fig. 14. Hit rate with respect to SINR for different collision scenarios.

It would be highly beneficial to investigate the advantages of the proposed sparse transmission, both with and without increased transmit power per chirp, in reducing interference to victim radars employing uniform transmission. Fig. 15(a) shows an example with two targets in the field of view of a victim radar with normalized amplitudes $\alpha_1 = 1$ and $\alpha_2 = 0.01$, ranges $r_1 = 20$ m and $r_2 = 5$ m, and velocities $v_1 = 15$ m/s and $v_2 = 10$ m/s, and azimuth angles $\theta_1 = 15^\circ$ and $\theta_2 = 37^\circ$. Fig. 15(b) shows that, when both the host and the victim FMCW radars use uniform transmission and interference exists in the whole CPI, the targets cannot be identified from the range–Doppler spectrum of the victim radar due to the high interference power. As shown in Fig. 15(c), after applying the gating technique to clip the interference with a high amplitude, the target with a small RCS is still embedded under the noise floor. We also utilize the singular value decomposition (SVD) method as a comparative scheme because of its proven superiority in eliminating interference signals within the received signal, as outlined in [70]. For the mth chirp, the received data of the victim radar with N channels are $\mathbf{Y} = \mathbf{Y}_s + \mathbf{Y}_i \in \mathbb{C}^{I \times N}$, where $\mathbf{Y}_s$, and $\mathbf{Y}_i$ are targets and interference samples, respectively. The received signal covariance matrix is $\mathbf{R} = \mathbf{Y}\mathbf{Y}^H$. Typically, the incident power of the interfering radar to the victim radar is much higher than the power received from the target because of the direct path between the interfering and the victim radars. Therefore, the principal component of the SVD of $\mathbf{R}$, expressed by eigenvalue s_1 and eigenvector $\mathbf{U}(:, 1)$, is regarded as the contribution of the interfering radar. In this case, the interference is suppressed by orthogonal subspace projection. The resulting

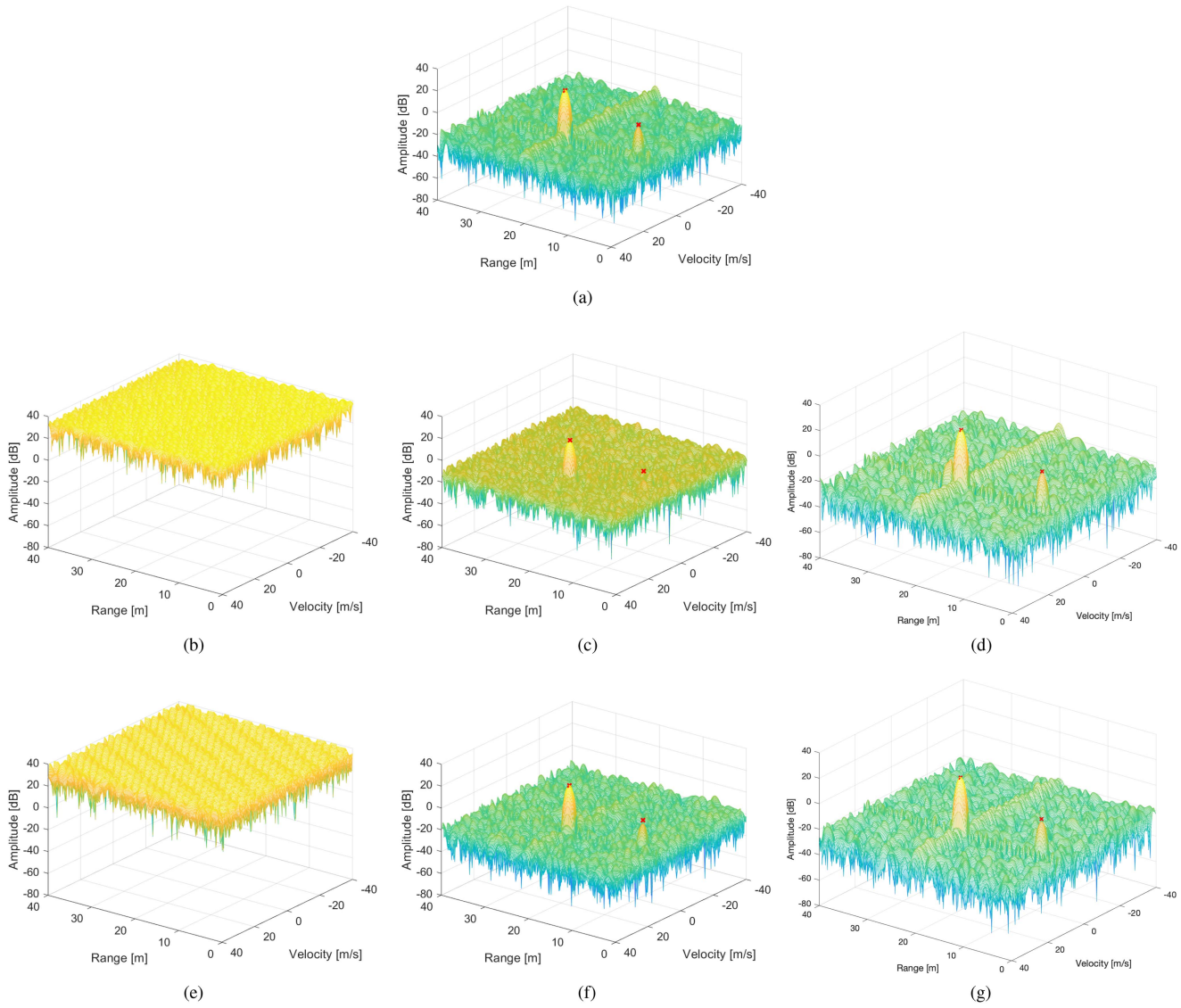

Fig. 15. Range–Doppler spectrum of victim radar, where × denotes the ground truth. (a) Targets plus noise. (b) Target plus interference and noise under the conventional uniform transmission before gating. (c) Same as (b), but after gating. (d) Same as (b), but after SVD mitigation. (e) Target plus interference and noise under the nested co-chirp transmission before gating. (f) Same as (e), but after gating. (g) Same as (e), but after SVD mitigation.

interference-free signal is expressed as $\hat{\mathbf{Y}} = \mathbf{P}_{\perp}\mathbf{Y}$, where $\mathbf{P}_{\perp} = \mathbf{I} - \mathbf{U}(:, 1)\mathbf{U}^{H}(:, 1)$, and $\mathbf{I}$ is the identity matrix. This method effectively restores the data matrix of the target signal with high precision.

Fig. 15(d) shows the case when the interference signal energy is strong and the target dynamic range is large. Although the target with a small RCS can be distinguished with the help of SVD technique, its strength is nevertheless very close to the sidelobe signal level of the large RCS target. On the other hand, as shown in Fig. 15(f), with co-chirps, the entire spectrum is free of interference. The target with a smaller RCS is clearly distinguished, and it demonstrates that the SVD method is superior to gating. Now, the host radar adopts the proposed sparse transmission following the nested co-chirp scheme with an increased transmit power to achieve the same processing gain as the uniform transmission scheme. Fig. 15(e) shows that, before gating, the targets are buried by the increased noise in the range–Doppler spectrum. However, after gating or SVD interference mitigation, the weaker target is clearly detected, as shown in Fig. 15(f) and (g). This is because only a much smaller number of chirps are corrupted under the sparse transmission scheme compared to the uniform transmission scheme.

Although sparse transmission can reduce the interference to other radar systems, increasing the power of a single chirp in order to obtain a processing gain similar to the traditional transmission method will cause higher electromagnetic pollution. Therefore, it is crucial to investigate how the increased chirp power impacts the radar illumination range. As introduced in [71], the linear gains of the transmitting and receiving antennas of an ultra-short-range radar (USRR) and a medium-range radar (MRR) are 4 and 10, respectively. At the same time, the RCS of the vehicle is

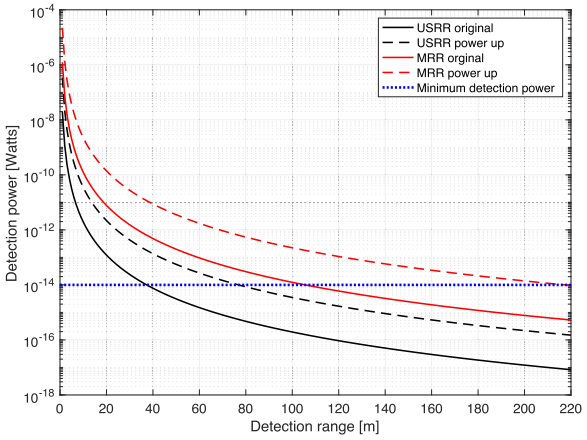

Fig. 16. Radar detection range versus power per chirp.

TABLE III
TI Radar Settings for Field Experiment

Parameter	Value
Carrier frequency, f_c	77 GHz
Maximum detection range, $R_{\max}$	25 m
Maximum detection velocity, $V_{\max}$	22 km/h
Bandwidth, B	3.12 GHz

10 dBsm. Therefore, in the traditional transmission mode, the RF output power is 12 dBm and the minimum detection power of the receiving chain is -110 dBm. Taking into account the aforementioned link budget and observing the relationship between the received power and the detection distance, as depicted in Fig. 16, it becomes evident that an increase in the chirp power can effectively extend the radar illumination distance. This implies that the transmission in the co-chirp mode amplifies the range of radar radiation.

To further compare the power interference range of the traditional chirp and co-chirp transmission methods, we set up victim radars V1, V2, V3, and V4 at distances of 100, 150, 200, and 250 m, respectively, from the interference radar. Targets were located at 20 and 5 m within the range of each victim radar with the RCS of 10 and 0.1 dBsm, respectively. Fig. 17 shows that with the conventional transmission, the victim radar is not required to perform any interference mitigation beyond 250 m; the two goals can be easily distinguished. However, the power of each chirp is now greater than in the co-chirp mode, and hence, the smaller RCS target is still submerged in noise. In other words, for the co-chirp radar, with its greater range, more radars need to perform interference mitigation.

C. Field Campaign Results

A TI imaging radar [68] is used in our field experiment, and its configuration is given in Table III. The simple scenario is shown in Fig. 18(a), where two pedestrians walk within the radar field of view with different velocities. The collected data consisted of 306 chirps in a conventional transmission with uniform PRI. Following the nested transmission, total $N_1 = N_2 = 17$ chirps are extracted from the

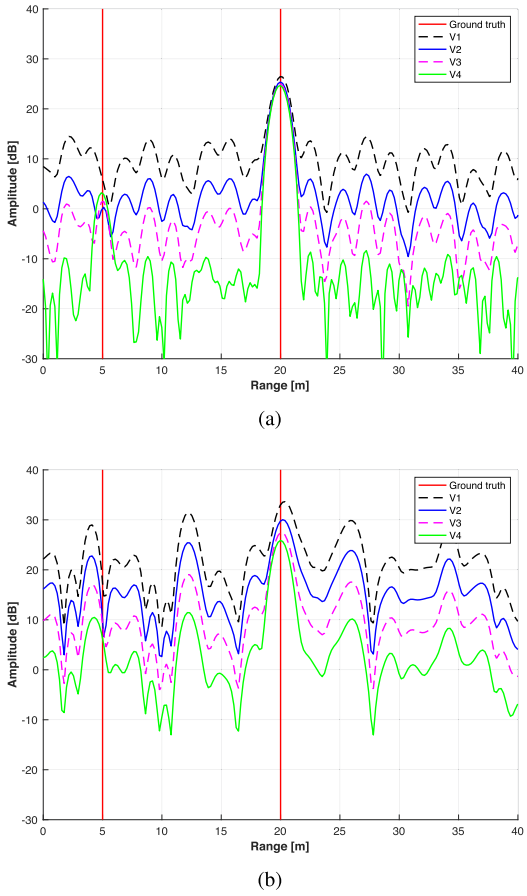

Fig. 17. Range profiles of victim radars at various distances without interference mitigation in (a) conventional chirp and (b) nested co-chirp transmission.

consecutive measurement to form an equivalent observation window as the conventional uniform PRI one.

Fig. 18(b) shows the range–Doppler spectrum obtained by performing 512-point FFTs along fast time and slow time of collected data from consecutive transmissions. In this figure, two targets are located at different ranges with distinct velocities, and the light pole is also labeled. The energy leakage from transmitters to receivers will result in a peak corresponding to the first few range bin indices in the range–Doppler spectrum. Since the range frequency f_R defined in (7) is proportional to the range of target [5], a high-pass filter has been implemented to suppress the leakage from transmitters before range–Doppler processing. The nonuniform FFT spectrum on nested data is shown in Fig. 18(c), where it is hard to tell the targets from the 2-D spectrum because of the high sidelobes. The constant false alarm rate method is used to detect range candidates r_{fft} from the range spectrum. Following the same way, we selected velocity candidates v_{fft} from the Doppler spectrum. Then, the range candidates r_{fft} and velocity candidates v_{fft} are exported into boost 2-D CS to pair. Many spurious peaks exist in Fig. 18(d) because the number of targets is overestimated when dealing with pairing. Fig. 18(e) shows that two pedestrians and a light pole are estimated correctly after dealiasing.

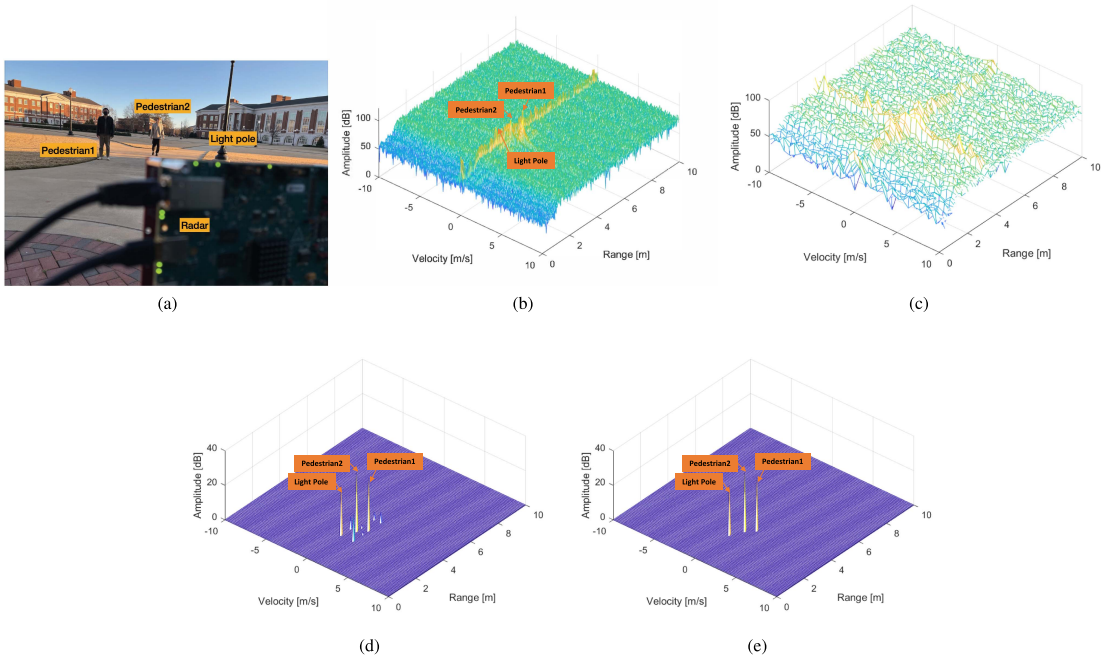

Fig. 18. Difference co-chirp FMCW radar field experiment. (a) Experiment scenario. (b) Nonuniform FFT range–Doppler spectrum from nested measurement. (c) FFT performed on collected consecutive data. (d) Boost pairing CS spectrum in nested transmission without dealiasing. (e) Boost pairing CS spectrum in nested transmission after dealiasing.

VI. CONCLUSION

In this article, we presented a difference co-chirp-based nonuniform PRI automotive FMCW radar, which is shown to achieve the same range–Doppler estimation performance as conventional FMCW radar with uniform PRI while significantly reducing the total number of chirps along slow time. Based on the constructed covariance matrix with fast-time samples as snapshots, the Doppler estimation has been estimated efficiently with FFT. A boosted 2-D CS algorithm followed by a Doppler dealiasing step was proposed to pair the range–Doppler estimation for multiple targets and filter out any spurious peaks, which has greatly reduced the computation cost of solving the pairing problem and completely avoided off-grid issues in CS. Numerical results demonstrated the feasibility of the proposed method. The robustness of the range–Doppler estimation under interference with different SINR levels was investigated. The radar field experiments revealed that the range and velocity of multiple targets can be estimated efficiently with high accuracy using the proposed boost 2-D CS technique.

APPENDIX A
PROOF OF THEOREM 1

Considering a rectangular pulse

$$x(t) = \text{Rect}\left(\frac{t}{T}\right), \quad -T/2 \leqslant t \leqslant T/2. \tag{28}$$

The complex AF, i.e., the matched filter output of $x(t)$ when there is a Doppler shift f_d, is

$$\widehat{A}(t, f_d) = \int_{-\infty}^{+\infty} x(s)x^*(s-t)e^{j2\pi f_d s}ds. \tag{29}$$

Following the definition in [72], the AF of rectangular pulse is the absolute value of $\widehat{A}(t, f_d)$, i.e.,

$$A(t, f_d) = \left|\widehat{A}(t, f_d)\right| = \left|\left(1 - \frac{|t|}{T}\right)\frac{\sin\left[\pi f_d(T-|t|)\right]}{\pi f_d(T-|t|)}\right|, \quad |t| \leqslant T. \tag{30}$$

The waveform of a single FM pulse is $\widehat{x}(t) = x(t)e^{j2\pi[f_c t + (B/2T)t^2]}$, and its complex AF is

$$\begin{aligned}\widehat{A}_{\text{fm}}(t, f_d) &= \int_{-\infty}^{+\infty} \widehat{x}(s)\widehat{x}^*(s-t)e^{j2\pi f_d s}ds \\ &= \int_{-\infty}^{+\infty} \left\{x(s)e^{j2\pi\left[f_c s + \frac{B}{2T}s^2\right]}\right. \\ &\quad \left.\cdot\, x^*(s-t)e^{-j2\pi\left[f_c(s-t) + \frac{B}{2T}(s-t)^2\right]}e^{j2\pi f_d s}\right\}ds \\ &= e^{j2\pi\left(f_c t - \frac{B}{2T}t^2\right)}\int_{-\infty}^{+\infty} x(s)x^*(s-t)e^{j2\pi\left(f_d + \frac{B}{T}t\right)s}ds \\ &= e^{j2\pi\left(f_c t - \frac{B}{2T}t^2\right)}\widehat{A}\left(t, f_d + \frac{B}{T}t\right).\end{aligned} \tag{31}$$

Therefore, the AF of an FM pulse is

$$\begin{aligned}A_{\text{fm}}(t, f_d) &= \left|\widehat{A}_{\text{fm}}(t, f_d)\right| \\ &= \left|\left(1 - \frac{|t|}{T}\right)\frac{\sin\left[\pi\left(f_d + \frac{B}{T}t\right)(T-|t|)\right]}{\pi\left(f_d + \frac{B}{T}t\right)(T-|t|)}\right|, \quad |t| \leqslant T.\end{aligned} \tag{32}$$

Compared with the rectangular pulse AF $A(t, f_d)$, only the Doppler term is changed in the FM pulse AF $A_{\text{fm}}(t, f_d)$.

A pulse burst can be exploited to increase the Doppler resolution. For M burst pulses, it holds that

$$\widehat{A}_b(t, f_d)=\int_{-\infty}^{+\infty}\sum_{m=0}^{M-1}x(s-mT)\sum_{n=0}^{M-1}x^*(s-t-nT)e^{j2\pi f_d s}ds.$$

Replacing $s-mT$ with $\hat{s}$, it holds that

$$\begin{aligned}&\widehat{A}_b(t, f_d)\\&=\int_{-\infty}^{+\infty}\sum_{m=0}^{M-1}x(\hat{s})\sum_{n=0}^{M-1}x^*(\hat{s}+(m-n)T-t)e^{j2\pi f_d\hat{s}}e^{j2\pi f_d mT}d\hat{s}\\&=\sum_{m=0}^{M-1}e^{j2\pi f_d mT}\sum_{n=0}^{M-1}\int_{-\infty}^{+\infty}x(\hat{s})x^*(\hat{s}-[t-(m-n)T])e^{j2\pi f_d\hat{s}}d\hat{s}\\&=\sum_{m=0}^{M-1}e^{j2\pi f_d mT}\sum_{n=0}^{M-1}\widehat{A}(t-(m-n)T, f_d)\end{aligned}\tag{33}$$

Let $m-n=\hat{n}$. For some function $F(m, n)$, it is well known that the following equation holds [73]:

$$\begin{aligned}\sum_{m=0}^{M-1}\sum_{n=0}^{M-1}F[m, n]=&\sum_{\hat{n}=-(M-1)}^{0}\sum_{m=0}^{M-|\hat{n}|-1}F[m, m-\hat{n}]\\&+\sum_{\hat{n}=1}^{M-1}\sum_{m=0}^{M-|\hat{n}|-1}F[m+\hat{n}, m].\end{aligned}\tag{34}$$

Therefore

$$\begin{aligned}\widehat{A}_b(t, f_d)=&\sum_{\hat{n}=-(M-1)}^{0}\widehat{A}(t-\hat{n}T, f_d)\sum_{m=0}^{M-|\hat{n}|-1}e^{j2\pi f_d mT}\\&+\sum_{\hat{n}=1}^{M-1}e^{j2\pi f_d\hat{n}T}\widehat{A}(t-\hat{n}T, f_d)\sum_{m=0}^{M-|\hat{n}|-1}e^{j2\pi f_d mT}.\end{aligned}$$

With the sum of geometric series, it holds that

$$\begin{aligned}\sum_{m=0}^{M-|\hat{n}|-1}e^{j2\pi f_d mT}&=\frac{1-e^{j2\pi f_d T[M-|\hat{n}|]}}{1-e^{j2\pi f_d T}}\\&=e^{j\pi f_d T(M-|\hat{n}|-1)}\frac{\sin\left(\pi f_d(M-|\hat{n}|)T\right)}{\sin(\pi f_d T)}.\end{aligned}$$

Thus

$$\widehat{A}_b(t, f_d)=\sum_{\hat{n}=-(M-1)}^{M-1}\widehat{A}(t-\hat{n}T, f_d)e^{j\pi f_d T(M+\hat{n}-1)}\frac{\sin(\pi f_d(M-|\hat{n}|)T)}{\sin(\pi f_d T)}.$$

As a result, the AF of a simple pulse train is

$$A_b(t, f_d)=\sum_{\hat{n}=-(M-1)}^{M-1}A(t-\hat{n}T, f_d)\left|\frac{\sin(\pi f_d(M-|\hat{n}|)T)}{\sin(\pi f_d T)}\right|.\tag{35}$$

Then, the AF of the burst FM pulse train is

$$\begin{aligned}&A_{\text{bfm}}(t, f_d)=A_b\left(t, f_d+\frac{B}{T}t\right)\\&=\sum_{\hat{n}=-(M-1)}^{\hat{n}=M-1}A\left(t-\hat{n}T, f_d+\frac{B}{T}t\right)\left|\frac{\sin(\pi(f_d+\frac{B}{T}t)(M-|\hat{n}|)T)}{\sin(\pi(f_d+\frac{B}{T}t)T)}\right|.\end{aligned}\tag{36}$$

Nonuniform chirp waveform under the nested transmission includes two groups of uniform chirps with different PRIs. The number of chirps in the first and second groups is N_1 and N_2 with PRI of T and $(N_1+1)T$, respectively. For the nested-chirp waveforms, it holds

$$\begin{aligned}&\widehat{A}_{\text{nested}}(t, f_d)\\&=\int_{-\infty}^{+\infty}\sum_{m=0}^{N_1-1}\widehat{x}(s-mT)\sum_{n=0}^{N_1-1}\widehat{x}^*(s-t-nT)e^{j2\pi f_d s}ds\\&+\int_{-\infty}^{+\infty}\left\{\sum_{m=0}^{N_2-1}\widehat{x}(s-(m+1)(N_1+1)T)\right.\\&\left.\cdot\sum_{n=0}^{N_2-1}\widehat{x}^*(s-t-(n+1)(N_1+1)T)e^{j2\pi f_d s}\right\}ds.\end{aligned}\tag{37}$$

Define $\hat{T}=(N_1+1)T$. It follows from (36) that (38) and (39) shown at the bottom of this page, hold.

Therefore, the AF of nested-chirp waveform is obtained as (15). Similarly, nonuniform chirp waveform under coprime transmission includes two overlapped groups of uniform chirp sequences with PRIs of T_1 and T_2, respectively. In

$$\left|\int_{-\infty}^{+\infty}\sum_{m=0}^{N_1-1}\widehat{x}(s-mT)\sum_{n=0}^{N_1-1}\widehat{x}^*(s-t-nT)e^{j2\pi f_d s}ds\right|=\sum_{p=-(N_1-1)}^{N_1-1}A\left(t-pT, f_d+\frac{B}{T}t\right)\left|\frac{\sin\left(\pi(f_d+\frac{B}{T}t)(N_1-|p|)T\right)}{\sin\left(\pi(f_d+\frac{B}{T}t)T\right)}\right|.\tag{38}$$

$$\begin{aligned}&\left|\int_{-\infty}^{+\infty}\sum_{m=0}^{N_2-1}\widehat{x}(s-(m+1)\hat{T})\sum_{n=0}^{N_2-1}\widehat{x}^*(s-t-(n+1)\hat{T})e^{j2\pi f_d s}ds\right|\\&=\sum_{q=-(N_2-1)}^{N_2-1}A\left(t-qT, f_d+\frac{B}{\hat{T}}t\right)\left|\frac{\sin\left(\pi(f_d+\frac{B}{\hat{T}}t)(N_2-|q|)\hat{T}\right)}{\sin\left(\pi(f_d+\frac{B}{\hat{T}}t)\hat{T}\right)}\right|.\end{aligned}\tag{39}$$

a similar way, the AF of coprime chirp waveform is obtained as in (16), which concludes the proof. □

REFERENCES

[1] L. Xu, S. Sun, and K. V. Mishra, "Difference co-chirps-based non-uniform PRF automotive FMCW radar," in *Proc. IEEE Int. Conf. Auton. Syst.*, 2021, pp. 1–5.

[2] S. Patole, M. Torlak, D. Wang, and M. Ali, "Automotive radars: A review of signal processing techniques," *IEEE Signal Process. Mag.*, vol. 34, no. 2, pp. 22–35, Mar. 2017.

[3] F. Engels, P. Heidenreich, A. M. Zoubir, F. K. Jondral, and M. Wintermantel, "Advances in automotive radar: A framework on computationally efficient high-resolution frequency estimation," *IEEE Signal Process. Mag.*, vol. 34, no. 2, pp. 36–46, Mar. 2017.

[4] K. V. Mishra, M. B. Shankar, V. Koivunen, B. Ottersten, and S. A. Vorobyov, "Toward millimeter-wave joint radar communications: A signal processing perspective," *IEEE Signal Process. Mag.*, vol. 36, no. 5, pp. 100–114, Sep. 2019.

[5] S. Sun, A. P. Petropulu, and H. V. Poor, "MIMO radar for advanced driver-assistance systems and autonomous driving: Advantages and challenges," *IEEE Signal Process. Mag.*, vol. 37, no. 4, pp. 98–117, Jul. 2020.

[6] C. Waldschmidt, J. Hasch, and W. Menzel, "Automotive radar—From first efforts to future systems," *IEEE J. Microw.*, vol. 1, no. 1, pp. 135–148, Jan. 2021.

[7] S. Sun and Y. D. Zhang, "4D automotive radar sensing for autonomous vehicles: A sparsity-oriented approach," *IEEE J. Sel. Topics Signal Process.*, vol. 15, no. 4, pp. 879–891, Jun. 2021.

[8] G. Duggal, S. Vishwakarma, K. V. Mishra, and S. S. Ram, "Doppler-resilient 802.11ad-based ultrashort range automotive joint radar-communications system," *IEEE Trans. Aerosp. Electron. Syst.*, vol. 56, no. 5, pp. 4035–4048, Oct. 2020.

[9] S. Alland, W. Stark, M. Ali, and A. Hedge, "Interference in automotive radar systems: Characteristics, mitigation techniques, and future research," *IEEE Signal Process. Mag.*, vol. 36, no. 5, pp. 45–59, Sep. 2019.

[10] M. Toth, P. Meissner, A. Melzer, and K. Witrisal, "Performance comparison of mutual automotive radar interference mitigation algorithms," in *Proc. IEEE Radar Conf.*, 2019, pp. 1–6.

[11] K. V. Mishra, S. Mulleti, and Y. C. Eldar, "RaSSteR: Random sparse step-frequency radar," 2020, *arXiv:2004.05720*.

[12] K. V. Mishra and Y. C. Eldar, "Sub-Nyquist radar: Principles and prototypes," in *Compressed Sensing in Radar Signal Processing*, A. D. Maio, Y. C. Eldar, and A. Haimovich, Eds. Cambridge, U.K.: Cambridge Univ. Press, 2019, pp. 1–48.

[13] S. Na, K. V. Mishra, Y. Liu, Y. C. Eldar, and X. Wang, "TenDSuR: Tensor-based 4D sub-Nyquist radar," *IEEE Signal Process. Lett.*, vol. 26, no. 2, pp. 237–241, Feb. 2019.

[14] J. Khoury, R. Ramanathan, D. McCloskey, R. Smith, and T. Campbell, "RadarMAC: Mitigating radar interference in self-driving cars," in *Proc. IEEE Int. Conf. Sens., Commun., Netw.*, 2016, pp. 1–9.

[15] P. Liu, Y. Liu, T. Huang, Y. Lu, and X. Wang, "Decentralized automotive radar spectrum allocation to avoid mutual interference using reinforcement learning," *IEEE Trans. Aerosp. Electron. Syst.*, vol. 57, no. 1, pp. 190–205, Feb. 2021.

[16] S. Jin and S. Roy, "FMCW radar network: Multiple access and interference mitigation," *IEEE J. Sel. Topics Signal Process.*, vol. 15, no. 4, pp. 968–979, Jun. 2021.

[17] M. W. Maier, "Non-uniform PRI pulse-Doppler radar," in *Proc. IEEE Southeastern Symp. Syst. Theory*, 1993, pp. 164–168.

[18] J. Li and Z. Chen, "Research on random PRI PD radar target velocity estimate based on NUFFT," in *Proc. IEEE CIE Int. Conf. Radar*, 2011, pp. 1801–1803.

[19] W. P. du Plessis, "Simultaneous unambiguous range and Doppler through non-uniform sampling," in *Proc. IEEE Radar Conf.*, 2020, pp. 1–6.

[20] P. P. Vaidyanathan and P. Pal, "Sparse sensing with co-prime samplers and arrays," *IEEE Trans. Signal Process.*, vol. 59, no. 2, pp. 573–586, Feb. 2011.

[21] A. Moffet, "Minimum-redundancy linear arrays," *IEEE Trans. Antennas Propag.*, vol. 16, no. 2, pp. 172–175, Mar. 1968.

[22] C.-Y. Chen and P. P. Vaidyanathan, "Minimum redundancy MIMO radars," in *Proc. IEEE Int. Symp. Circuits Syst.*, 2008, pp. 45–48.

[23] P. Pal and P. P. Vaidyanathan, "Nested arrays: A novel approach to array processing with enhanced degrees of freedom," *IEEE Trans. Signal Process.*, vol. 58, no. 8, pp. 4167–4181, Aug. 2010.

[24] C.-L. Liu and P. P. Vaidyanathan, "Remarks on the spatial smoothing step in coarray MUSIC," *IEEE Signal Process. Lett.*, vol. 22, no. 9, pp. 1438–1442, Sep. 2015.

[25] S. Qin, Y. D. Zhang, and M. G. Amin, "Generalized coprime array configurations for direction-of-arrival estimation," *IEEE Trans. Signal Process.*, vol. 63, no. 6, pp. 1377–1390, Mar. 2015.

[26] M. Wang and A. Nehorai, "Coarrays, MUSIC, and the Cramér-Rao bound," *IEEE Trans. Signal Process.*, vol. 65, no. 4, pp. 933–946, Feb. 2017.

[27] S. Qin, Y. D. Zhang, M. G. Amin, and A. M. Zoubir, "Generalized coprime sampling of Toeplitz matrices for spectrum estimation," *IEEE Trans. Signal Process.*, vol. 65, no. 1, pp. 81–94, Jan. 2016.

[28] W. Lv, K. V. Mishra, and S. Chen, "Co-pulsing FDA radar," *IEEE Trans. Aerosp. Electron. Syst.*, vol. 59, no. 2, pp. 1107–1126, Apr. 2023.

[29] I. Bilik, O. Longman, S. Villeval, and J. Tabrikian, "The rise of radar for autonomous vehicles: Signal processing solutions and future research directions," *IEEE Signal Process. Mag.*, vol. 36, no. 5, pp. 20–31, Sep. 2019.

[30] Y. Chi, L. L. Scharf, A. Pezeshki, and A. R. Calderbank, "Sensitivity to basis mismatch in compressed sensing," *IEEE Trans. Signal Process.*, vol. 59, no. 5, pp. 2182–2195, May 2011.

[31] K. V. Mishra, M. Cho, A. Kruger, and W. Xu, "Spectral super-resolution with prior knowledge," *IEEE Trans. Signal Process.*, vol. 63, no. 20, pp. 5342–5357, Oct. 2015.

[32] S. Lee, Y.-J. Yoon, J. Yoon, H. Sim, and S.-C. Kim, "Periodic clutter suppression in iron road structures for automotive radar systems," *IET Radar, Sonar, Navigat.*, vol. 12, no. 10, pp. 1146–1153, 2018.

[33] Y.-Z. Ma, C. Cui, B.-S. Kim, J.-M. Joo, S. H. Jeon, and S. Nam, "Road clutter spectrum of BSD FMCW automotive radar," in *Proc. Eur. Radar Conf.*, 2015, pp. 109–112.

[34] P. Vouras, "Fully adaptive space-time processing on nested arrays," in *Proc. IEEE Radar Conf.*, 2015, pp. 858–863.

[35] Y. Zhou, Y. Li, and L. Wang, "The space-time adaptive processing method in airborne MIMO radar with nested structure," in *Proc. IEEE 4th Int. Conf. Signal Image Process.*, 2019, pp. 485–489.

[36] X. Wang, Z. Yang, and J. Huang, "Space-time adaptive processing for clutter suppression in coprime array and coprime pulse repetition interval airborne radar," in *Proc. Int. Symp. Intell. Signal Process. Commun. Syst.*, 2017, pp. 380–385.

[37] R. Molina-Masegosa and J. Gozalvez, "LTE-V for sidelink 5G V2X vehicular communications: A new 5G technology for short-range vehicle-to-everything communications," *IEEE Veh. Technol. Mag.*, vol. 12, no. 4, pp. 30–39, Dec. 2017.

[38] J. B. Kenney, "Dedicated short-range communications (DSRC) standards in the United States," *Proc. IEEE*, vol. 99, no. 7, pp. 1162–1182, Jul. 2011.

[39] F. Lyu et al., "Characterizing urban vehicle-to-vehicle communications for reliable safety applications," *IEEE Trans. Intell. Transp. Syst.*, vol. 21, no. 6, pp. 2586–2602, Jun. 2020.

[40] O. Simeone, U. Spagnolini, Y. Bar-Ness, and S. H. Strogatz, "Distributed synchronization in wireless networks," *IEEE Signal Process. Mag.*, vol. 25, no. 5, pp. 81–97, Sep. 2008.

[41] S. Sedighi, K. V. Mishra, M. R. B. Shankar, and B. Ottersten, "Localization with one-bit passive radars in narrowband Internet-of-Things using multivariate polynomial optimization," *IEEE Trans. Signal Process.*, vol. 69, pp. 2525–2540, 2021.

[42] F. Lampel et al., "System level synchronization of phase-coded FMCW automotive radars for RadCom," in *Proc. 14th Eur. Conf. Antennas Propag.*, 2020, pp. 1–5.
[43] A. K. Karthik and R. S. Blum, "Recent advances in clock synchronization for packet-switched networks," *Found. Trends Signal Process.*, vol. 13, no. 4, pp. 360–443, 2020.
[44] J. M. Merlo, S. R. Mghabghab, and J. A. Nanzer, "Wireless picosecond time synchronization for distributed antenna arrays," *IEEE Trans. Microw. Theory Techn.*, vol. 71, no. 4, pp. 1720–1731, Apr. 2023.
[45] S. R. Mghabghab, A. Schlegel, and J. A. Nanzer, "Adaptive distributed transceiver synchronization over a 90 m microwave wireless link," *IEEE Trans. Antennas Propag.*, vol. 70, no. 5, pp. 3688–3699, May 2022.
[46] M. A. Hadi, S. Alshebeili, K. Jamil, and F. E. A. El-Samie, "Compressive sensing applied to radar systems: An overview," *Signal, Image Video Process.*, vol. 9, pp. 25–39, 2015.
[47] L. Anitori, A. Maleki, M. Otten, R. G. Baraniuk, and P. Hoogeboom, "Design and analysis of compressed sensing radar detectors," *IEEE Trans. Signal Process.*, vol. 61, no. 4, pp. 813–827, Feb. 2013.
[48] FCC Office of Engineering and Technology, "Amendment of sections 15.35 and 15.253 of the commission's rules regarding operation of radar systems in the 76–77 GHz band and amendment of section 15.253 of the commission's rules to permit fixed use of radar in the 76-77 GHz band," Federal Communications Commission, Washington, DC, USA, Tech. Rep. 27 FCC Rcd 7880, May 2012.
[49] A. Ruddle, "Preliminary estimates of electromagnetic field exposures due to advanced vehicle technologies," in *Proc. Loughborough Antennas Propag. Conf.*, 2016, pp. 1–5.
[50] International Commission on Non-Ionizing Radiation Protection, "Guidelines for limiting exposure to time-varying electric, magnetic, and electromagnetic fields (up to 300 GHz)," *Health Phys.*, vol. 74, no. 4, pp. 494–521, 1998.
[51] C. Baylis, L. Cohen, D. Eustice, and R. Marks, "Myths concerning Woodward's ambiguity function: Analysis and resolution," *IEEE Trans. Aerosp. Electron. Syst.*, vol. 52, no. 6, pp. 2886–2895, Dec. 2016.
[52] S. Pinilla, K. V. Mishra, B. M. Sadler, and H. Arguello, "Phase retrieval for radar waveform design," 2022, *arXiv:2201.11384*.
[53] M. Jankiraman, *Design of Multi-Frequency CW Radars*. Rijeka, Croatia: SciTech, 2007.
[54] C. Zhou, Y. Gu, X. Fan, Z. Shi, G. Mao, and Y. D. Zhang, "Direction-of-arrival estimation for coprime array via virtual array interpolation," *IEEE Trans. Signal Process.*, vol. 66, no. 22, pp. 5956–5971, Nov. 2018.
[55] S. Zhang, A. Ahmed, Y. D. Zhang, and S. Sun, "Enhanced DOA estimation exploiting multi-frequency sparse array," *IEEE Trans. Signal Process.*, vol. 69, pp. 5935–5946, 2021.
[56] A. Gupta, U. Madhow, and A. Arbabian, "Super-resolution in position and velocity estimation for short-range MM-wave radar," in *Proc. Asilomar Conf. Signals, Syst. Comput.*, 2016, pp. 1144–1148.
[57] M. M. Hyder and K. Mahata, "Range-Doppler imaging via sparse representation," in *Proc. IEEE Radar Conf.*, 2011, pp. 486–491.
[58] E. J. Candès and T. Tao, "The Dantzig selector: Statistical estimation when p is much larger than n," *Ann. Statist.*, vol. 35, no. 6, pp. 2313–2351, 2007.
[59] T. T. Cai and L. Wang, "Orthogonal matching pursuit for sparse signal recovery with noise," *IEEE Trans. Inf. Theory*, vol. 57, no. 7, pp. 4680–4688, Jul. 2011.
[60] E. Candès and J. Romberg, "Sparsity and incoherence in compressive sampling," *Inverse Probl.*, vol. 23, no. 3, 2007, Art. no. 969.
[61] L. Carin, D. Liu, and B. Guo, "Coherence, compressive sensing, and random sensor arrays," *IEEE Antennas Propag. Mag.*, vol. 53, no. 4, pp. 28–39, Aug. 2011.
[62] B. Mailhé, R. Gribonval, F. Bimbot, and P. Vandergheynst, "A low complexity orthogonal matching pursuit for sparse signal approximation with shift-invariant dictionaries," in *Proc. IEEE Int. Conf. Acoust., Speech Signal Process.*, 2009, pp. 3445–3448.
[63] T. Fei, H. Guang, Y. Sun, C. Grimm, and E. Warsitz, "An efficient sparse sensing based interference mitigation approach for automotive radar," in *Proc. 17th Eur. Radar Conf.*, 2021, pp. 274–277.
[64] R. Schmidt, "Multiple emitter location and signal parameter estimation," *IEEE Trans. Antennas Propag.*, vol. AP-34, no. 3, pp. 276–280, Mar. 1986.
[65] R. Roy and T. Kailath, "ESPRIT—Estimation of signal parameters via rotation invariance techniques," *IEEE Trans. Acoust., Speech, Signal Process.*, vol. 17, no. 7, pp. 984–995, Jul. 1989.
[66] W. Roberts, P. Stoica, J. Li, T. Yardibi, and F. Sadjadi, "Iterative adaptive approaches to MIMO radar imaging," *IEEE J. Sel. Topics Signal Process.*, vol. 4, no. 1, pp. 5–20, Feb. 2010.
[67] S. Sun and Y. D. Zhang, "Four-dimensional high-resolution automotive radar imaging exploiting joint sparse-frequency and sparse-array design," in *Proc. IEEE Int. Conf. Acoust., Speech, Signal Process.*, 2021, pp. 8413–8417.
[68] *Design Guide: TIDEP-01012 Imaging Radar Using Cascaded MmWave Sensor Reference Design*, Rev. ATexas Instrum., Dallas, TX, USA, 2020. [Online]. Available: https://www.ti.com/lit/ug/tiduen5a/tiduen5a.pdf
[69] Continental Automotive, Hanover, Germany. Accessed: Sep. 2022. [Online]. Available: https://www.continental-automotive.com
[70] S. Sun and C. Alcalde, "Removing interference from signals received by detectors supported on a vehicle," U.S. Patent App. 16/292 432, Sep. 10 2020.
[71] *Radar Services in the 76–81 GHz Band Report and Order*, Federal Communications Commission, Washington, DC, USA, 2017.
[72] M. A. Richards, *Fundamentals of Radar Signal Processing*, 2nd ed. New York, NY, USA: McGraw-Hill, 2014.
[73] A. W. Rihaczek, *Principles of High-Resolution Radar*. Norwood, MA, USA: Artech House, 1996.

Lifan Xu (Student Member, IEEE) received the B.S. degree in electrical engineering from Shihezi University, Shihezi, China, in 2016, and the M.S. degree in electrical engineering from the Chinese Academy of Sciences, Beijing, China, in 2019. He is currently working toward the Ph.D. degree in automotive radar signal processing with the Department of Electrical and Computer Engineering, The University of Alabama, Tuscaloosa, AL, USA.

His research interests include automotive radar, radar signal processing, multiple-input multiple-output radar with sparse sensing, and machine learning.

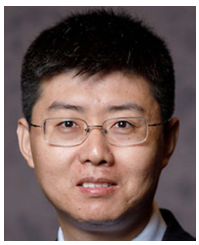

Shunqiao Sun (Senior Member, IEEE) received the Ph.D. degree in electrical and computer engineering from Rutgers, The State University of New Jersey, New Brunswick, NJ, USA, in 2016.

From 2016 to 2019, he was with the radar core team of Aptiv, Technical Center Malibu, Malibu, CA, USA, where he has worked on advanced radar signal processing and machine learning algorithms for self-driving vehicles and lead the development of direction-of-arrival estimation techniques for next-generation short-range radar sensor, which has been used in over 120-million automotive radar units. He is currently an Assistant Professor with The University of Alabama, Tuscaloosa, AL, USA. His research interests include the interface of statistical and sparse signal processing with mathematical optimizations, automotive radar, multiple-input multiple-output radar, machine learning, and smart sensing for autonomous vehicles.

Dr. Sun has been awarded the 2016 IEEE Aerospace and Electronic Systems Society Robert T. Hill Best Dissertation Award for his thesis "MIMO radar with Sparse Sensing." He coauthored a paper that received the Best Student Paper Award at 2020 IEEE Sensor Array and Multichannel Signal Processing Workshop. He is the Vice-Chair of IEEE Signal Processing Society Autonomous Systems Initiative (for the period 2023–2024). He is an Associate Editor for IEEE SIGNAL PROCESSING LETTERS and IEEE OPEN JOURNAL OF SIGNAL PROCESSING.

Kumar Vijay Mishra (Senior Member, IEEE) received the B.Tech. (Gold Medal, Hons.) degree (*summa cum laude*) in electronics and communication engineering from the National Institute of Technology, Hamirpur, India, in 2003, the M.S. degree in electrical engineering from Colorado State University, Fort Collins, CO, USA, in 2012, and the M.S. degree in mathematics and the Ph.D. degree in electrical engineering from The University of Iowa, Iowa City, IA, USA, in 2015.

He has worked on NASA's Global Precipitation Mission Ground Validation weather radars. He is currently a Senior Fellow with the U.S. Army Research Laboratory, Adelphi, MD, USA, a Technical Adviser to Singapore-based automotive radar start-up Hertzwell and Boston-based imaging radar startup Aura Intelligent Systems, and an Honorary Research Fellow of Interdisciplinary Centre for Security, Reliability and Trust, University of Luxembourg, Esch-sur-Alzette, Luxembourg. Previously, he had research appointments at Electronics and Radar Development Establishment, Defence Research and Development Organisation, Bengaluru, India; Hydroscience and Engineering, Iowa City; Mitsubishi Electric Research Labs, Cambridge, MA, USA; Qualcomm, San Jose, CA; and Technion—Israel Institute of Technology, Haifa, Israel. He is the Lead Co-Editor for three upcoming books on radar: *Signal Processing for Joint Radar Communications* (Hoboken, NJ, USA: Wiley-IEEE Press, 2023), *Next-Generation Cognitive Radar Systems* (Radar, Electromagnetics & Signal Processing Technologies Series) (London, U.K.: IET Press), and *Advances in Weather Radar* (Radar, Electromagnetics & Signal Processing Technologies Series, vols. 1–3) (London, U.K.: IET Press). His research interests include radar systems, signal processing, remote sensing, and electromagnetics.

Dr. Mishra is the Distinguished Lecturer of IEEE Communications Society (for the period 2023–2024), IEEE Aerospace and Electronic Systems Society (AESS) (for the period 2023–2024), and IEEE Vehicular Technology Society (for the period 2023–2024). He was the Distinguished Lecturer of IEEE Future Networks Initiative in 2022. He was the recipient of the IET Premium Best Paper Prize in 2021, the U.S. National Academies Harry Diamond Distinguished Fellowship from 2018 to 2021, the American Geophysical Union Editors' Citation for Excellence in 2019, the Royal Meteorological Society Quarterly Journal Editor's Prize in 2017, the Viterbi Postdoctoral Fellowship in 2015 and 2016, the Lady Davis Postdoctoral Fellowship in 2017, the DRDO LRDE Scientist of the Year Award in 2006, the NITH Director's Gold Medal in 2003, and the NITH Best Student Award in 2003. He has received Best Paper Awards at 2019 IEEE International Workshop on Machine Learning for Signal Processing and 2019 IEEE International Applied Computational Electromagnetics Society Symposium. Since 2023, he has been a Chair of the Synthetic Apertures Technical Working Group of IEEE Signal Processing Society (SPS). Since 2021, he has been a Vice-Chair of IEEE Synthetic Aperture Standards Committee, which is the first SPS standards committee. Since 2021, he has been the Vice-Chair of the International Union of Radio Science Commission C, where he is also a Chair designate for the period 2023–2026. He has been an Elected Member of three technical committees of the IEEE SPS: Signal Processing for Communications and Networking Technical Committee, Sensor Array and Multichannel Technical Committee, and Applied Signal Processing Systems Technical Committee, and IEEE AESS Radar Systems Panel. Since 2020, he has been an Associate Editor for IEEE TRANSACTIONS ON AEROSPACE AND ELECTRONIC SYSTEMS, where he was awarded Outstanding Editor recognition in 2021. He was a Lead/Guest Editor for several special issues in journals, such as *IEEE Signal Processing Magazine*, IEEE JOURNAL OF SELECTED TOPICS IN SIGNAL PROCESSING, and IEEE JOURNAL ON SELECTED AREAS IN COMMUNICATIONS.

Yimin D. Zhang (Fellow, IEEE) received the Ph.D. degree in applied physics from the University of Tsukuba, Tsukuba, Japan, in 1988.

He is currently an Associate Professor with the Department of Electrical and Computer Engineering, Temple University, Philadelphia, PA, USA. His research interests include array signal processing, compressive sensing, machine learning, convex optimization, and time–frequency analysis with applications to radar, wireless communications, and satellite navigation.

Dr. Zhang is a Senior Area Editor for IEEE TRANSACTIONS ON SIGNAL PROCESSING and an Associate Editor for *Signal Processing*. He was also an Associate Editor for IEEE TRANSACTIONS ON SIGNAL PROCESSING, IEEE TRANSACTIONS ON AEROSPACE AND ELECTRONIC SYSTEMS, IEEE SIGNAL PROCESSING LETTERS, and *Journal of the Franklin Institute*. He was a Technical Co-Chair of 2018 IEEE Sensor Array and Multichannel Signal Processing Workshop. He was the recipient of the 2016 IET Radar, Sonar & Navigation Premium Award, the 2017 IEEE Aerospace and Electronic Systems Society Harry Rowe Mimno Award, the 2019 IET Communications Premium Award, and the 2021 EURASIP Best Paper Award for Signal Processing. He coauthored two papers that respectively received the 2018 and 2021 IEEE Signal Processing Society Young Author Best Paper Awards. He is a Fellow of SPIE (the International Society for Optics and Photonics).